

RICE UNIVERSITY

Concentric Nanoshells and Plasmon Hybridization

by

Corey J. Radloff

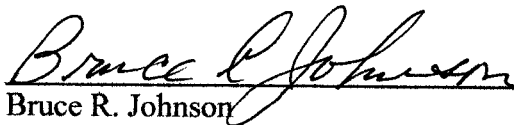
A THESIS SUBMITTED
IN PARTIAL FULFILLMENT OF THE
REQUIREMENTS FOR THE DEGREE

Doctor of Philosophy

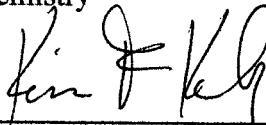
APPROVED THESIS COMMITTEE:



Naomi J. Halas, Chair
Stanley C. Moore Professor in Electrical and
Computer Engineering
Professor of Chemistry



Bruce R. Johnson
Senior Faculty Fellow
Chemistry



Kevin F. Kelly
Assistant Professor of Electrical and
Computer Engineering

HOUSTON, TEXAS

JUNE 2003

UMI Number: 3122525

INFORMATION TO USERS

The quality of this reproduction is dependent upon the quality of the copy submitted. Broken or indistinct print, colored or poor quality illustrations and photographs, print bleed-through, substandard margins, and improper alignment can adversely affect reproduction.

In the unlikely event that the author did not send a complete manuscript and there are missing pages, these will be noted. Also, if unauthorized copyright material had to be removed, a note will indicate the deletion.



UMI Microform 3122525

Copyright 2004 by ProQuest Information and Learning Company.

All rights reserved. This microform edition is protected against unauthorized copying under Title 17, United States Code.

ProQuest Information and Learning Company
300 North Zeeb Road
P.O. Box 1346
Ann Arbor, MI 48106-1346

Abstract

Concentric Nanoshells and Plasmon Hybridization

Corey J. Radloff

The optical properties of metal nanostructures are related to their plasmon response, which is sensitively dependent on nanostructure geometry and environment. The metallodielectric, core-shell structure of nanoshells represents a unique geometry allowing for the systematic tunability of the plasmon resonance of the nanostructure. This is accomplished by varying the relative dimensions of the core and shell layers. Fabrication of a nanoshell particle with a strong plasmon resonance is dependent on shell quality, which is strongly dependent on the careful preparation of the metal shell. The resonant response of metal nanostructures can also be modified through plasmon-plasmon interactions. This work focuses on the fabrication of nanoparticles with a multi-layer, concentric-shell structure consisting of a silica core, inner gold shell layer, silica spacer layer, and an outer gold shell layer. This concentric nanoshell particle is fabricated through the controlled growth of a nanometer-scale silica layer around a preformed nanoshell. The silica layer was found to increase the thermal and chemical stability of the nanoshell particles. A second gold shell could be grown on this layer to generate the concentric nanoshell particle. This layered nanoparticle geometry has a plasmon resonance dependent on the interaction between the inner and outer shell plasmons. This interaction can be explained in terms of a sphere-cavity model of plasmon hybridization derived from a semi-classical model of the plasmon resonance. Varying the dimensions of the concentric shell layers can independently and

systematically control the plasmon resonance of the inner and outer shell, which effects the interaction between the two plasmons. The coupling between the inner and outer shell plasmons was investigated experimentally by varying the concentric nanoshell dimensions, specifically examining how the spectral detuning of the inner and outer shell resonances and spatial interaction between inner and outer shell plasmons determine the nanoparticle's optical properties. Calculations using Mie scattering theory to model the nanoshell plasmon response agree quantitatively with experimental measurements of the nanoshell plasmon resonance in both the single-layer and multi-layer regime.

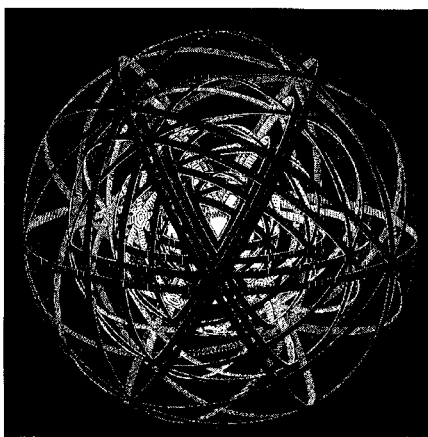
Acknowledgements

Thanks to all the members of the Halas group, past and present, especially Steve, Sarah, and Kevin for being great mentors and colleagues. Thanks to Naomi for bringing out my best and providing an environment where I could become a good scientist.

Thanks to my family and friends who supported me in my efforts even when the only thing they understood was my desire to make it through this process. Especially my mother who is one of the people who appreciates what it means to get a Ph.D. and has shown me an unlimited amount of patience and understanding during the pursuit of this work. Thanks to Cristin for being my friend, colleague, and wife. You have been my strongest supporter, without you this would have been a long and painful process.

Finally I would like to dedicate this work to my father. My only regret is that he could not be here to see me finish. His curiosity and fascination with the world are an inspiration to my scientific endeavors.

**In loving memory
John C. Radloff
1935 – 2001**



("Concentric Rinds" M.C. Escher, 1953)

Contents

Abstract	ii
Acknowledgements	iv
Table of Contents	v
List of Figures	vii
List of Tables	x

Chapter I: Introduction **1**

Chapter II: Theory **5**

2.1 Introduction	5
2.2 Light Absorption by Colloids: the quasi-static limit	5
2.3 Light Scattering by Metallodielectric Nanospheres	10
2.4 Plasmon Hybridization in Nanoshells and Concentric Nanoshells	12

Chapter III: Fabrication of Concentric Metal Nanoshells **20**

3.1 Introduction	20
3.2 Metal Nanoshell Fabrication	22
3.3 Concentric Nanoshell Fabrication	29
3.4 Reducing Agents	36

Chapter IV: Enhanced Thermal Stability of Silica-encapsulated Gold

Nanoshells **39**

4.1 Introduction	39
4.2 Nanoshell Preparation	41
4.3 Spectroscopic Effects of Thermal Treatment	42
4.4 Structural Effects of Thermal Treatment	43
4.5 Summary	45

Chapter V: Chemical Stability of Metal Nanoshells **47**

5.1 Introduction	47
5.2 Nanoshell Preparation	48

5.3 Gold Shell Decomposition in CCl_4	50
5.4 Effect of Solvent and Shell Structure on Decomposition	52
5.5 Reactivity of Primary Amines with CCl_4	54
5.6 Characterization of Amine- CCl_4 Reaction	55
5.7 Conclusions	56
Chapter VI: Optical Properties of Concentric Metal Nanoshells	57
6.1 Introduction	57
6.2 Mie Scattering Theory for a Concentric Nanoshell	62
6.3 Sample Preparation	68
6.4 Results and Discussion	69
6.5 Summary	74
Chapter VII: Nanoshell Deposition and Arrays	75
7.1 Introduction	75
7.2 Electric-Field Assisted Deposition of Metal Nanoshells	77
7.3 Electrostatic Deposition of Metal Nanoshells	82
7.4 Summary	87
Chapter VIII: Summary and Impact	89
Bibliography	93

Figures

Figure 2.1: Schematic illustration of a core-shell particle	9
Figure 2.2: Theoretical and measured nanoshell extinction spectra	12
Figure 2.3: Schematic illustration of the polarizations in a metal film and nanoshell	13
Figure 2.4: Energy level diagram depicting the plasmon hybridization in terms of the sphere-cavity model	14
Figure 2.5: Extinction spectra for nanoshells calculated with different dielectric functions	17
Figure 2.6: Energy level diagram and schematic of the concentric nanoshell system	19
Figure 3.1: A schematic illustrating the fabrication of a concentric nanoshell	21
Figure 3.2: TEM images of silica cores seeded from different THPC-Au solutions	28
Figure 3.3: SEM images of gold nanoshells	29
Figure 3.4: TEM images of thin silica layer growth around a gold nanoshell	33
Figure 3.5: Electron microscope images of silica-encapsulated gold nanoshells	35
Figure 3.6: SEM images depicting the concentric shell fabrication process	36
Figure 3.7: UV/Vis spectra of gold nanoshells grown using different reducing agents	38
Figure 4.1: Typical absorbance spectrum for silica coated gold nanoshells	41

Figure 4.2: Absorbance spectra for silica coated gold nanoshells exposed to different temperatures	42
Figure 4.3: SEM images of different nanoshells showing the effect of heating at 325 °C	44
Figure 5.1: Typical gold nanoshells	48
Figure 5.2: Concentric sphere nanoshell particles before and after dispersal in CCl ₄	49
Figure 5.3: SEM images and extinction spectra of gold nanoshells before and after dispersal in CCl ₄	51
Figure 5.4: Incomplete nanoshell particles before and after dispersal in CCl ₄	54
Figure 6.1: Schematic illustrating the concept of the concentric nanoshell	59
Figure 6.2: Simplified energy level diagram of the plasmon hybridization in a concentric nanoshell	60
Figure 6.3: Theoretical calculations showing the plasmon response of different nanoshell particles and concentric nanoshells constructed from the single-layer nanoshells	62
Figure 6.4: Theoretical calculations depicting the separation dependence of the concentric nanoshell plasmon	63
Figure 6.5: Summary of theoretical calculations of the effects on concentric plasmon peak position	64
Figure 6.6: Near-field maps for concentric nanoshells taken as a slice through the particle	65
Figure 6.7: Graph of the difference in peak position between the symmetric and	

anti-symmetric modes of the concentric nanoshell plasmon	66
Figure 6.8: SEM images depicting the concentric nanoshell fabrication process	69
Figure 6.9: Experimentally measured peak plasmon positions compared to the theoretically predicted hybrid plasmon modes	70
Figure 6.10: Experimental and theoretical extinction spectra for concentric nanoshells in the strong and weak-coupling regimes	71
Figure 6.11: Theoretical extinction spectrum of the strong-coupling regime plotted with multipole components	72
Figure 6.12: The theoretical and measured extinction spectra for a concentric nanoshell when there is no coupling	73
Figure 7.1: Schematic of an electrodeposition cell and graphs of the sedimentation rate	79
Figure 7.2: SEM images of gold nanoshells electrodeposited in ordered and disordered films	80
Figure 7.3: Extinction spectra for gold nanoshells in films	81
Figure 7.4: Picture of electrodeposited films of gold nanoshells	82
Figure 7.5: Schematic depicting the electrostatic deposition of nanoshells onto a flat substrate.	83
Figure 7.6: Extinction spectra and AFM images of electrostaticly deposited nanoshells	84

Tables

Table 3.1: Table of different Stöber reaction volumes.

25

Chapter I: Introduction

The emergent field of plasmonics seeks to engineer, on the nanoscale, the electro-optical interaction between metal nanostructures and their surroundings.¹⁻⁵ The goal of this type of nanoscale engineering is to harness the plasmon resonance of the metal nanostructure in order to enhance or compliment the properties of the coupled system. The plasmon resonance is due to the collective excitation of the electrons in the metal at a specific frequency determined by the material properties and geometry of the nanostructure. This is extremely useful in designing nanoparticles for surface enhanced Raman spectroscopy,⁶⁻⁸ fluorescent enhancement, thermal interactions,⁹⁻¹² and surface plasmon resonance sensing.^{3,5}

Metal nanoshells represent a unique nanostructure ideally suited to nanoscale plasmonic engineering. They are metallodielectric nanoparticles with a dielectric core and a metal shell that have a geometry dependent plasmon resonance. The plasmon resonance is accurately described by existing theory allowing one to design a particle with a specific size, composition, and plasmon resonance.^{13,14} Because of the geometry dependent plasmon resonance of the nanoshell, varying the core-shell dimensions of the particle allows one to access frequencies in the electromagnetic spectrum from the visible to the infrared. The simple fabrication chemistry, their relative ease in processing, and their highly symmetric geometry compared to other plasmonic structures, such as nanorods, make nanoshells viable candidates for incorporation into a wide range of applications that would benefit from the interaction with their strong plasmon resonance. Metal

nanoshells are currently fabricated using inorganic materials, specifically, with a silica core and a gold or silver shell.

Silica nanoparticles are used as core substrates and can be made easily as spheres from ~80 nm to > 1 micron in diameter with good monodispersity (5 – 10 % standard deviation).¹⁵⁻¹⁷ Silica is attractive as a core substrate because it is an optically transparent material that is easily fabricated and whose surface is easily derivatized. While the silica particles can be made relatively monodisperse, to produce highly monodisperse particle solutions requires strict monitoring of reactant purity and cleanliness of glassware. This becomes important for nanoshells in order to minimize line broadening of the plasmon resonance and for ordered assembly of nanoshell particles. The silica surface is easily derivatized with alkoxysilane molecules with various functional head groups (amine, thiol, carboxylate). The core is derivatized with an amine functionality and the particles are “seeded” using small gold colloid as nucleation sites for the electroless reduction of the metal shell. This results in a thin metal shell layer surrounding the particle. A dense coverage of gold particles on the silica surface determines the minimum thickness and completeness of the shell layer. To insure a dense coverage, the ionic strength of the gold colloid solution can be increased in order to decrease the repulsive Coloumbic forces between the gold particles. This allows the particles to densely pack onto the silica surface.

Once the metal shell is grown the surface can be derivatized using a host of molecular species. Due to the strong affinity of thiols for gold or silver surfaces, these molecules

can easily attach to the nanoshells in solution. This allows for the transfer of the nanoshells into a host of non-polar solvents. A more complex surface treatment of the nanoshells involves the growth of a silica encapsulation layer around the particle. This layer offers increased thermal stability and improves the ability to manipulate the nanoshells into arrays or films. The silica encapsulation shell also provides a substrate for the growth of a concentric nanoshell particle. A concentric nanoshell particle has a 4-layer geometry with a dielectric-metal-dielectric-metal composition. This presents a unique platform for the investigation of plasmon-plasmon interactions.

Recent quantum mechanical theoretical investigations into the nature of the nanoshell plasmon resonance have shown that a strong interaction, or hybridization, between plasmons associated with the outer (sphere) and inner (cavity) surfaces of the metal shell layer is responsible for the plasmon tunability of nanoshells.¹⁸ The application of a semi-classical approach to model the nanoshell plasmon resonance revealed two eigenmodes within the nanoshell plasmon associated with the symmetric and anti-symmetric polarizations of the sphere and cavity surfaces. The symmetric mode is found in the visible to infrared region of the electromagnetic spectrum and is observed in the measured extinction spectrum of metal nanoshells. However, the anti-symmetric mode is found in the ultra-violet region of the spectrum and cannot easily be resolved due to interband transitions in the metal that occur at these frequencies. However, the concentric nanoshell particle presents a means to study these polarization interactions. Because of the multi-layer geometry, it is possible to observe the hybrid plasmon resonance resulting from the interaction between the symmetric polarizations of the two

metal shells. Experimental evidence has shown this plasmon-plasmon coupling to follow the same trends as the cavity-sphere interaction predicted theoretically for a nanoshell particle. The new modes arising from the coupling of the symmetric modes of the two shells are easily observed in the visible to infrared region of the spectrum.

In this work the fabrication of concentric nanoshells and the observation of a strong plasmon hybridization effect in the concentric shell geometry will be discussed. Chapter 2 will outline the electrostatic model of the plasmon resonance and the application of a previously developed formalism for calculating the plasmon response of metal nanoshells and concentric nanoshells. Chapter 3 will discuss techniques applied to the growth of gold nanoshells and the fabrication of concentric nanoshell particles. Chapters 4 and 5 will discuss the chemical and thermal stability of metal nanoshells. Chapter 6 will discuss the experimental observation of the hybrid plasmon resonance in concentric nanoshell particles and includes a comparison to the electrostatic description of the plasmon-plasmon interaction. The manipulation of nanoshells into arrays and films will be discussed in Chapter 7.

Chapter II: Theory

2.1 Introduction

The theoretical foundation of the interaction between light and spherical particles, developed by Gustav Mie, was developed in the early part of the 20th century.¹³ This application of classical electromagnetic theory allows for the complete modeling of the diffraction of a plane wave by a homogeneous sphere of arbitrary size and composition embedded in a homogeneous medium. Aden and Kerker later expanded Mie scattering theory for the description of a spherical particle having a core-shell geometry.¹⁴ In the quasi-static limit, where the particles are small compared to the wavelength of incident light (diameter $\ll \lambda$), the complete solution to Mie scattering theory is significantly simplified. However, in the case of metal nanoshells and concentric nanoshells, realistic particle sizes are well beyond this limit and phase retardation effects make a significant contribution to the shape and position of the particle's plasmon resonance. As such, a generalized vector basis function solution to Maxwell's equations is used to generate a complete electrostatic model of the nanoshell interaction with light.

2.2 Light Absorption by Colloids: the quasi-static limit

For a dilute colloidal solution the particle concentration and extinction cross-section can be related to the attenuation of light through the solution using the Beer-Lambert law:

$$A = \log_{10} \frac{I_0}{I} = \frac{N\sigma_{ext}l}{2.303} \quad (2.1)$$

where A is the absorbance measured experimentally and related to the transmission of light through the sample, N is the number of particles per unit volume, l is the path length through the sample, and σ_{ext} the extinction cross-section of a particle. The extinction cross-section is a measure of the total interaction of light with the particle. This includes scattering of light where photons are absorbed and re-emitted by the particle. The extinction also includes absorption, which is the conversion of light to heat. For a spherical particle made of a material with a complex, frequency-dependent dielectric function, $\varepsilon(\omega) = \varepsilon'(\omega) + i\varepsilon''(\omega)$, embedded in a non-absorbing medium with a dielectric constant, ε_m , the extinction cross-section is given as:

$$\sigma_{\text{ext}} = \frac{2\pi}{k^2} \sum (2n+1) \text{Re}(a_n + b_n) \quad (2.2)$$

where k is the wave-vector $2\pi/\lambda$. The terms a_n and b_n are the scattering coefficients, which are a function of particle size and of the frequency of light in terms of the Ricatti-Bessel functions.¹⁹⁻²² A similar relation can be used to determine the scattering cross-section of the particle:

$$\sigma_{\text{scatt}} = \frac{2\pi}{k^2} \sum (2n+1) \text{Re}(a_n^2 + b_n^2) \quad (2.3)$$

while the absorption cross-section can be derived from the extinction and scattering terms, $\sigma_{\text{abs}} = \sigma_{\text{ext}} - \sigma_{\text{scatt}}$. The summation index, n , is the order of the partial wave described by the vector spherical harmonic functions. The $n = 1$ term corresponds to an oscillating dipole when observing the particle in the far field and is labeled the dipole term. For particles within the quasi-static limit, this term dominates the series. In the quasi-static limit the small size of the particle with respect to the incident light allows the particle to experience a uniform electromagnetic field in time and space. However,

higher order terms in the summation are necessary to accurately describe particles beyond the quasi-static limit. These terms correspond to higher order multipoles, e.g. quadrupole ($n = 2$) and octupole ($n = 3$), which are due to phase retardation effects that will be discussed later. When considering particles in the quasi-static limit and taking into account only the $n = 1$ term, the extinction cross-section simplifies to:

$$\sigma_{ext} = \frac{24 \pi^2 R^3 \varepsilon_m^{\frac{3}{2}}}{\lambda} \frac{\varepsilon''(\omega)}{(\varepsilon'(\omega) + 2\varepsilon_m)^2 + \varepsilon''(\omega)^2} \quad (2.4)$$

where R is the radius of the particle. A strong absorption peak is realized from this equation when the resonance condition, $\varepsilon'(\omega) = -2\varepsilon_m$ ($\varepsilon''(\omega)$ is small), is met. For many metals, absorption in the electromagnetic spectrum up to the bulk plasmon frequency is dominated by free electron behavior. The dielectric response of the metal particle in the case of free electron behavior can be described using the Drude model.²³ In the Drude model a metal nanoparticle is considered as an electron gas dispersed throughout a solid sphere of positive charge. The metal atoms are fixed in place and possess a positive charge as the valence electrons are not specifically attached to any one atom and are free to roam within the metal. Using the Drude model the real and imaginary parts of the frequency dependent dielectric function can be written as:

$$\varepsilon'(\omega) = \varepsilon^\infty - \frac{\omega_p^2}{(\omega^2 + \omega_d^2)} \quad (2.5a, b)$$

$$\varepsilon''(\omega) = \frac{\omega_p^2 \omega_d}{\omega(\omega^2 + \omega_d^2)}$$

where ε^∞ is the high frequency dielectric constant due to interband and core transitions. The term ω_p is the bulk plasmon frequency, $\omega_p^2 = Ne^2/m\varepsilon_0$, where N is the concentration

of electrons and m is the effective mass of the electron. The term ω_d is the damping frequency, $\omega_d = v_f/R_{\text{bulk}}$, which is related to the mean free path of an electron (R_{bulk}) in the specific metal and the Fermi velocity of the electron (v_f). When the particle dimensions are smaller than the mean free path of the electron then the particle's radius must be added to the damping frequency to account for electron scattering by the particle's surface. With the introduction of equation (2.5a) it is evident that over the range of frequencies below the bulk plasmon frequency of the metal, $\epsilon'(\omega)$ has a negative value. This is because the electrons are oscillating out of phase with the electric field of the incident light wave. In a small metal particle the dipole oscillation sets up a surface polarization charge that acts as a restoring force on the free electron gas as it is forced to oscillate by the incoming wave. When the resonance condition is satisfied, the long wavelength absorption of the bulk material is condensed into a single surface plasmon resonance. The Drude model presents a powerful means of interpreting the optical absorption behavior of metal particles strictly in terms of the particle's material properties.

Another useful relation in understanding the optical resonances of metal nanoparticles is the static polarizability of the particle. For a homogeneous particle within the quasi-static limit the static polarizability is given as:

$$\alpha = 4\pi\epsilon_0 R^3 \frac{\epsilon'(\omega) + i\epsilon''(\omega) - \epsilon_m}{\epsilon'(\omega) + i\epsilon''(\omega) + 2\epsilon_m} \quad (2.6)$$

This term is also dependent on the material properties of the particle by inclusion of the complex dielectric function. The resonant frequency can be derived from this equation knowing the particle dimension. The plasmon resonance is observed when the resonance

condition stated earlier is applied to the static polarizability. When considering light scattering from a particle that has a heterogeneous composition consisting of concentric spheres of alternating materials an analytical solution can be derived. It is useful to begin the analysis of such a particle in the quasi-static limit to derive the basic optical properties without the complication of phase retardation effects. The dependence of the plasmon resonance on the nanoparticle dimensions can be found in the static polarizability of this new nanostructure. For a particle with a simple core-shell structure as shown in Figure 2.1, the polarizability is given as:

$$\alpha = 4\pi\epsilon_0 R_s^3 \frac{(\epsilon_s - \epsilon_m)(\epsilon_c + 2\epsilon_s) + (R_c/R_s)^3(\epsilon_c - \epsilon_s)(\epsilon_m + 2\epsilon_s)}{(\epsilon_s + 2\epsilon_m)(\epsilon_c + 2\epsilon_s) + (R_c/R_s)^3(\epsilon_c - \epsilon_s)(2\epsilon_s - \epsilon_m)} \quad (2.7)$$

where ϵ_c and ϵ_m are the dielectric constants of the core and medium, ϵ_s is the frequency-dependent, complex dielectric function of the shell material, R_c and R_s are the core and shell radii. From this equation the polarizability of the homogeneous particle can be derived when $\epsilon_c = \epsilon_s$ and $R_c = R_s$. When the resonance condition is applied to equation 7 the additional term of the core-shell ratio found in the polarizability introduces a geometry dependence on the location of the resonant frequency.

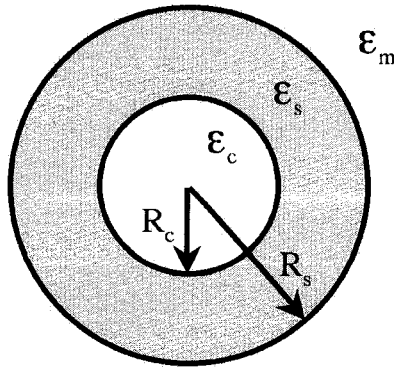


Figure 2.1: Schematic illustration of a core-shell particle.

2.3 Light Scattering by Metallodielectric Nanospheres

In order to accurately model the scattering of light by metal nanoshells it is necessary to move beyond the quasi-static limit presented in the last section. This is due to the constraints on fabrication of particles with dimensions that fall within the quasi-static limit. Current methods allow for the fabrication of nanoshell particles ranging from about 90 nm to > 1 micron in diameter, well beyond the quasi-static limit. In this size regime it becomes necessary to include phase retardation effects in any models of the interaction of light with the nanoshell particle.²⁴ Once the particle dimension is comparable to the wavelength of light the particle no longer experiences a uniform electromagnetic field. Phase retardation effects account for the broadening of the spectral linewidth of the plasmon resonance as well as the shift in resonance with increasing particle size. The effects of phase retardation are also responsible for the excitation of higher order multipoles ($n > 1$) in the plasmon resonance. Inclusion of higher order multipoles in the series expansion of the extinction cross-section results in secondary peaks, which arise in the plasmon resonance blue-shifted with respect to the main dipole resonance of the particle.

In this work a vector basis function solution to Maxwell's equations, described elsewhere in detail, is used when modeling the nanoshell response to electromagnetic stimulation.²⁵⁻²⁷ Advantages to this method include its efficient computation time and high degree of accuracy. To determine the scattering, absorption, and extinction cross-sections of a particle the electromagnetic fields of the incident wave, the scattered wave, and the wave

inside the particle are expanded using vector spherical harmonic basis functions: \mathbf{M} , \mathbf{N} , and \mathbf{L} . These three basis functions have been shown to be both orthogonal and complete. Because of the completeness of the set of basis functions any plane wave can be expressed as a series solution of the $\{\mathbf{L}, \mathbf{M}, \mathbf{N}\}$ set of vector functions. In describing the electromagnetic propagation through a layered particle three regimes must be modeled: the core-shell boundary, the boundary between two shells, and the shell-medium boundary. At the junction of each layer, the electromagnetic fields must satisfy Maxwell's boundary conditions whereby the waves are continuous across the junction. Since the nanoshell system is isotropic only the \mathbf{M} and \mathbf{N} functions are needed. The electromagnetic waves are expressed as a series solution of vector spherical harmonics expanded in terms of the \mathbf{M} and \mathbf{N} basis functions in all three regions:

$$\begin{aligned} E_i &= \sum_{n=1}^{\infty} \{a_n \mathbf{M}_n + b_n \mathbf{N}_n\} \\ H_i &= -i \sqrt{\frac{\epsilon_i}{\mu_i}} \sum_{n=1}^{\infty} \{a_n \mathbf{M}_n + b_n \mathbf{N}_n\} \end{aligned} \quad (2.8)$$

The subscript, i , refers to the region where the wave is evaluated. For nanoshell particles, the core region ($i = 1$) is evaluated using spherical Bessel functions. The region of the metal shell layer ($i = 2$) is evaluated using both spherical Bessel functions and Hankel functions and the region of the embedding medium ($i = 3$) uses only the Hankel functions. The formalism used allows for the convenient solution of Maxwell's equations for an infinite number of layers. The scattering coefficients (a_n and b_n) are used to calculate the far-field extinction, scattering, and absorption cross-sections of the particle. These coefficients can also be used to determine the local fields surrounding the particle.

To accurately model the extinction spectrum of a gold nanoshell particle the dielectric function used is derived from experimental data (n and k) collected by Johnson and Christy for gold films.²⁸ Figure 2.2 shows an extinction spectrum calculated using a dielectric function derived from the Johnson and Christy data, fit to a measured extinction spectrum of a gold nanoshell. The individual terms of the expansion series are plotted to show the importance of including higher order multipoles in the solution in order to accurately model the nanoshell response. The excellent agreement between the theoretical and experimental extinction spectra confirms the accuracy in the use of the vector basis function solution.

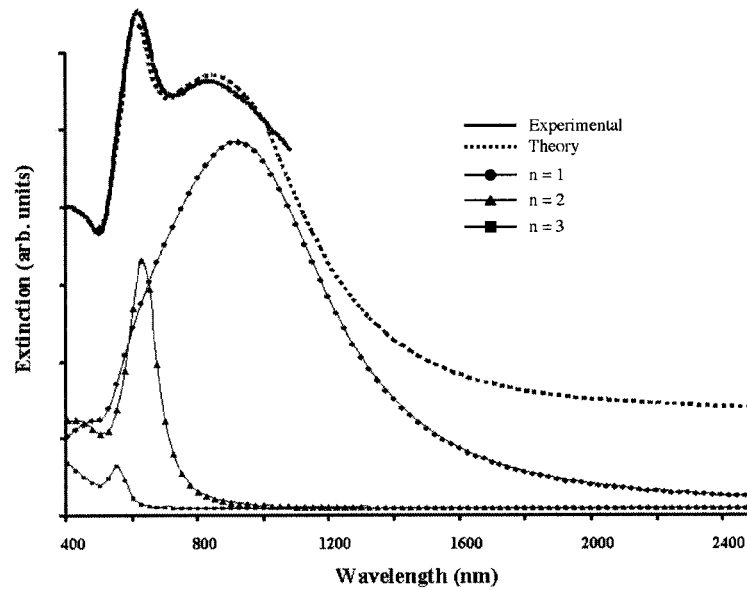


Figure 2.2: A theoretically calculated extinction spectrum (dashed line) fit to a measured nanoshell extinction spectrum (solid line). The $n = 1, 2, 3$ terms are plotted separately to illustrate the importance of including higher order multipoles in the calculation. The nanoshell dimensions are $R_c = 80$ nm, $R_s = 107$ nm, using a core and medium dielectric constant of $\epsilon_c = 2.04$ (silica), $\epsilon_m = 2.09$ (chloroform), respectively.

2.4 Plasmon Hybridization in Nanoshells and Concentric Nanoshells

When considering the origin of the plasmon resonance in a metal-dielectric composite structure it is useful to first begin with a thin planar metal layer surrounded by a dielectric medium. Under specific circumstances described by Raether,²⁹ it is possible to excite the surface plasmon of this structure. One can also observe a splitting of the surface plasmon into two eigenmodes due to a coupling between the structure's two boundaries described by the equation:

$$\omega_{\pm}^2 = \omega_p^2 \frac{1 \pm e^{-kd}}{(\epsilon_0 + \epsilon_s) \pm e^{-kd}(\epsilon_0 - \epsilon_s)} \quad (2.9)$$

A similar splitting of the plasmon resonance into two eigenmodes has been predicted for a particle with a metal shell around a dielectric core. If one considers a dielectric sphere coated by a metal shell, the splitting of the surface plasmon into two eigenmodes is the result of the difference in polarization between the particle's outer and inner surfaces. Figure 2.3 depicts the polarization modes for the planar surface and for a metal nanoshell structure.

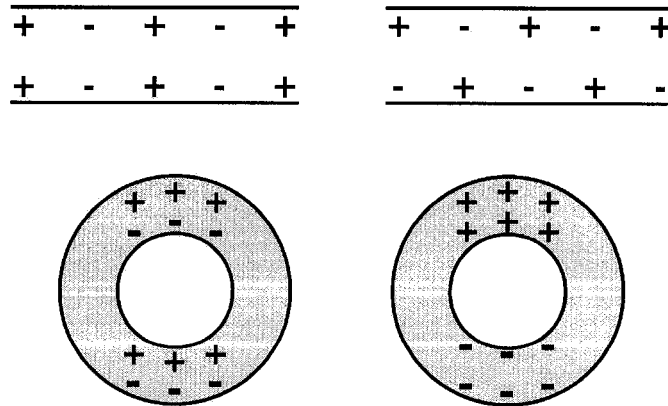


Figure 2.3: Schematic illustration of the possible polarizations for a metal film and a metal nanoshell.

Recently, a fully quantum mechanical model of the nanoshell response to incident electromagnetic radiation has been put forth.^{18,30} This model is based on a semi-classical approach typically used for molecular systems, such as C₆₀, which exhibit a core-shell electronic structure. For a spherical core-shell geometry the semi-classical approach predicts two plasmon oscillation modes consisting of a symmetric oscillation and an anti-symmetric oscillation. The energies of these modes are given by the equation:

$$\omega_{\pm}^2 = \omega_s^2 \left[1 \pm \frac{1}{2l+1} \sqrt{1 + 4l(l+1)x^{2l+1}} \right] \quad (2.10)$$

where ω_s is the surface plasmon energy and x is the core:shell ratio (R_c/R_s). Using this model the ω_+ mode has been assigned to the anti-symmetric polarization mode where the inner and outer surfaces of the particle are oppositely polarized, while the ω_- mode is assigned to the symmetric polarization mode. Using equation 2.10 it is possible to predict the relative locations of these two modes. The anti-symmetric mode is located at higher energies with respect to the symmetric mode. This is due to the increased excitation energy needed to oppositely polarize the different surfaces of the metal shell.

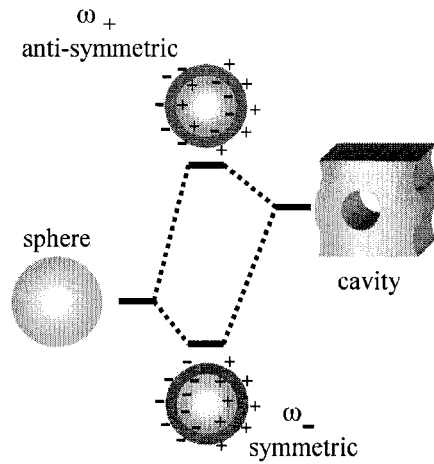


Figure 2.4: Energy level diagram depicting the plasmon hybridization in terms of the sphere-cavity model

The two eigenmodes of the metallodielectric nanoparticle arising from the core-shell structure have been assigned using a sphere-cavity physical model of the nanoparticle as depicted in Figure 2.4. In this physical model, the inner surface of the shell is considered as a cavity surface, while the outer surface of the shell is considered as a sphere surface. Each surface can support its own surface plasmon and the plasmon resonance of the nanoshell particle is the result of the hybridization of the simpler sphere and cavity sub-units. The positions of the two eigenmodes of the nanoshell plasmon are determined by the strength of the interaction between the sphere and cavity plasmons as a function of shell thickness.

While plasmon splitting in concentric sphere particles has been predicted using an electrostatic approach, only recently was the phenomenon seriously investigated using the semi-classical approach. The additional eigenmodes that arise from the coupling of the different metal surfaces have been theoretically described using an analytical formalism similar to the vector basis function solution.^{31,32} However, this description failed to accurately describe the nature of the plasmon splitting resulting in the hybrid eigenmodes. In using a fully electrostatic model, such as Drude, one can see the plasmon splitting resulting from the coupling between the sphere and cavity surfaces, but previous electrostatic simulations of the core-shell system failed to look explicitly for this effect. Simulations using an entirely electrostatic model of the nanoshell system also suffered by employing a dielectric function derived from the experimental data reported by Johnson and Christy. Typical calculations to model the plasmon response of metal nanoparticles, including the formalism used in this work, have used this data to derive the dielectric

function of the metal. These calculations have shown excellent agreement when compared to the experimentally measured plasmon response of gold nanoparticles and nanoshells as shown in Figure 2.2. Owing to this excellent agreement, most simulations use the Johnson and Christy data and in doing so fail to observe the plasmon hybridization described in semi-classical models. Both modes of the hybridized plasmon cannot be seen as the Johnson and Christy data does not extend far enough into the ultraviolet. Furthermore, the interband transitions found in gold at these frequencies prevent the clear resolution of the anti-symmetric mode. Even when modeling a particle using a Drude dielectric function the high frequency contribution (ϵ^∞) still accounts for the interband transitions in the metal. It is not until this high frequency contribution is removed that the ω_+ mode is unambiguously resolved.

Most simulations look at the spectral range from the visible to the mid-infrared. This corresponds to a range that is bounded in the visible by the strong interband transitions and extends into the infrared following the Johnson and Christy data. Figure 2.5(a) shows a comparison of the calculated extinction spectrum of a nanoshell when using the experimentally derived dielectric function or a Drude function. The Drude function excludes the effects of interband transitions in the metal and allows for the complete resolution of the hybrid plasmon resonance. In both spectra in Figure 2.5(a), the broadening mechanism associated with the nanoparticle dimension being smaller than the electron mean free path has been removed.²⁴ This accounts for the sharp peak widths and allows for ease in comparison between spectra. The symmetric mode of the nanoshell plasmon representing a symmetric polarization of the electrons in the gold shell

is seen at about 3.5 eV when calculated using the modified Drude dielectric function compared to about 2.5 eV using the Johnson and Christy derived dielectric function. This red-shift in the plasmon mode position is due to the effects of interband transitions, which are neglected in the Drude model, but considered when using the Johnson and Christy data. The full effects of the broadening mechanism and the interband transitions on the nature of plasmon hybridization will be compared in Chapter 6. The anti-symmetric mode can be seen at about 8.25 eV in the Drude model; however, the Johnson and Christy data does not extend to this region of the spectrum.

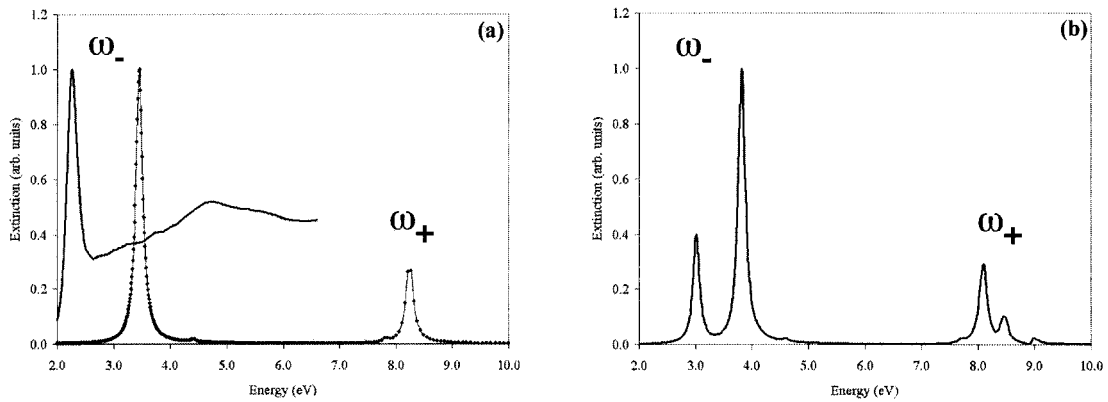


Figure 2.5: The calculated extinction spectra for (a) a nanoshell particle calculated with a Drude dielectric function (circles) and a dielectric function derived from experimental data (solid line). (b) The extinction spectrum calculated for a concentric nanoshell using the Drude function.

Conveniently, typical energies of the ω_- mode fall within the visible to infrared region of the electromagnetic spectrum, a region easily observed using commercially available spectrophotometers and corresponding to the Johnson and Christy data. As mentioned before the ω_+ mode is located in the ultraviolet region of the spectrum beyond the measurable range of typical spectrophotometers. Strong interband transitions would interfere with any spectral measurements taken in this region of the spectrum. This is due

to the overall increase in the magnitude of the interband transitions, which follows the overall increase in scattering due to larger nanoparticle diameters. This presents a challenging situation in order to observe the plasmon hybridization in a nanoshell system.

From Figure 2.5(b) it can be seen that the extinction spectrum from a concentric nanoshell particle exhibits a hybrid plasmon resonance owing to the coupling between each metal shell layer. The spectrum in Figure 2.5(b) is for a multi-layer particle assembled by embedding a smaller nanoshell within the core of the particle plotted in Figure 2.5(a). The plasmon-plasmon interaction, due to the metal shell coupling, results in a splitting of both the symmetric and anti-symmetric nanoshells peaks. This introduces a unique geometry for the experimental observation of plasmon hybridization. Because it is experimentally simple to make measurements in the visible to infrared region of the spectrum, it is possible to use a concentric sphere particle with a 4-layer, silica-gold-silica-gold composition to observe plasmon hybridization. This also allows for the application of Mie scattering theory to model the system using the previously described formalism discussed earlier in the chapter, which has already been shown to be in excellent agreement with experimental measurements of the plasmon resonance of nanoshell particles. The energy level diagram in Figure 2.6 depicts the hybridization of the concentric nanoshell plasmon in terms of the single shell plasmon interactions. The nature of the plasmon hybridization predicted by the sphere-cavity model can be applied to the concentric nanoshell system. The highlighted energy levels indicate the observable eigenmodes of the concentric nanoshell plasmon resonance.

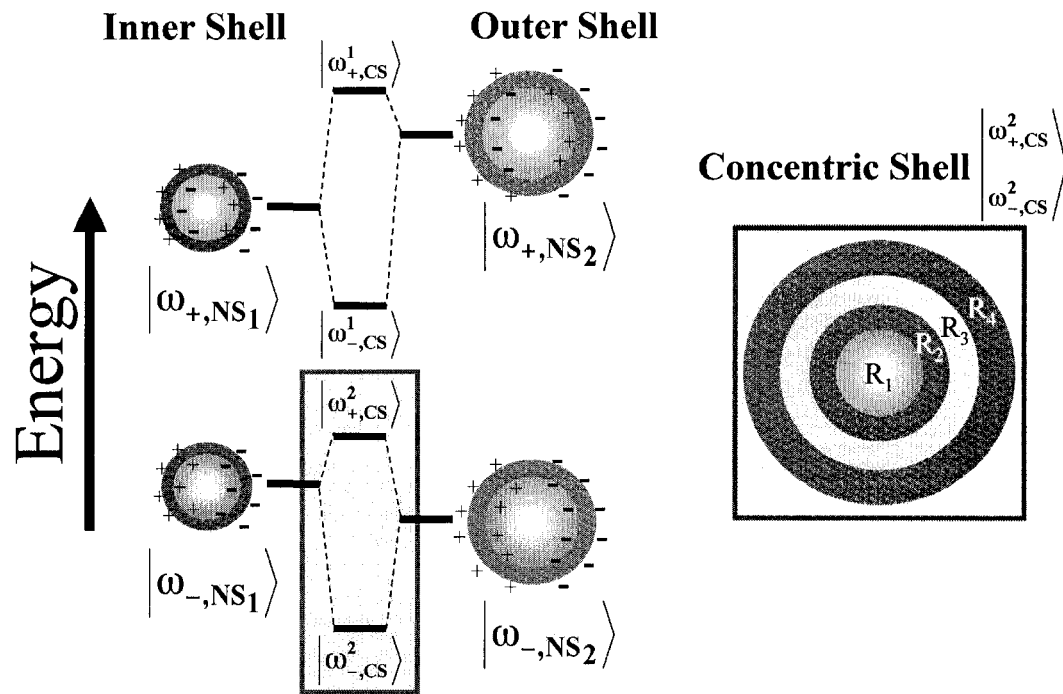


Figure 2.6: Energy level diagram and schematic of the concentric nanoshell system. The highlighted levels represent the experimentally observable eigenmodes.

Chapter III: Fabrication of Concentric Metal Nanoshells

3.1 Introduction

A concentric nanoshell is a nanoparticle with a multi-layer, dielectric-metal-dielectric-metal composition consisting of a smaller nanoshell embedded in the core of a larger nanoshell. Concentric nanoshells are fabricated using a preformed metal nanoshell substrate to construct a second metallodielectric double layer. A simplified fabrication scheme for the construction of concentric nanoshells is shown in Figure 3.1. Gold nanoshells are fabricated from a previously developed process using silica nanoparticles as substrates for electroless metal deposition.¹ The quality of nanoshells produced can be defined in terms of spectral quality and metal shell quality. Spectral quality, or the quality of the nanoshell solution, involves a strong plasmon resonance having clearly distinguished multipole resonances with minimum inhomogeneous broadening effects due to particle size distribution. Two important factors effecting the quality of the metal shell are: the “seeding” of the silica surface with small gold nanoparticles and the reducing agent used to grow the gold shell. In the former case the quality of shell is dependent on a dense coverage of the gold particles in order to grow a complete and thin shell. In the latter case choosing an appropriate reducing agent can insure shell quality in different size regimes.

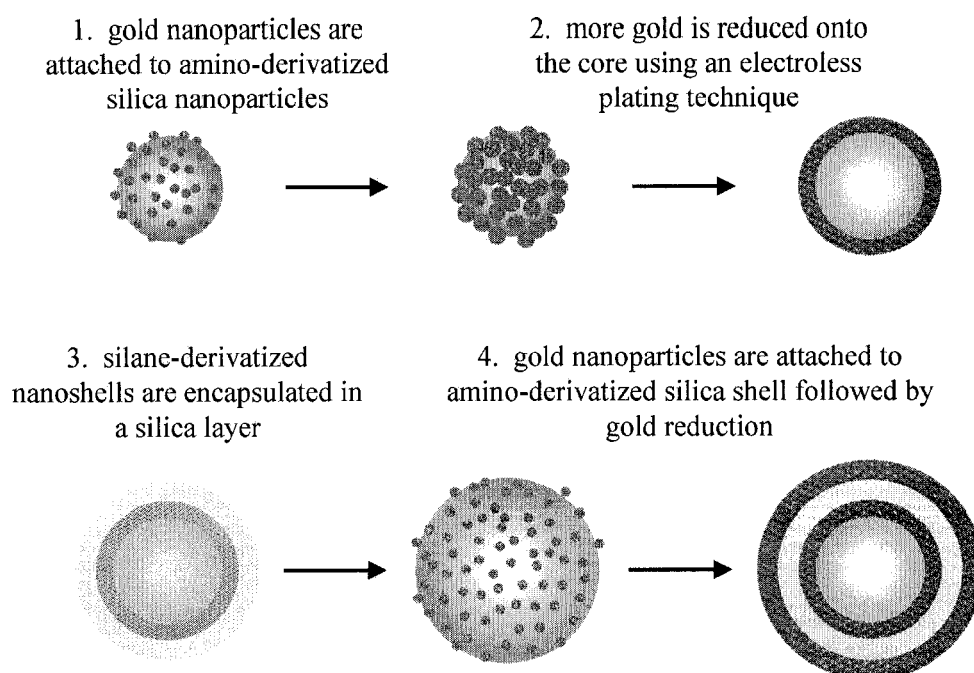


Figure 3.1: A schematic illustrating the steps involved in the fabrication of a concentric nanoshell.

The process of encapsulating the metal nanoshell surface with a dielectric layer for the deposition of a second metal shell is adapted from a process developed for encapsulating small gold colloid in silica.³³ This involves the surface functionalization of the gold shell through an amino moiety on an alkoxysilane molecule. This molecular layer acts as a precursor to the condensation of a thin silica shell from a silicate solution. Both steps in the silica-encapsulation process require strict control over pH and concentration of reactants. Challenges in adapting this process to nanoshells arise from the large size of the particles and the particle's sensitivity to solution chemistry. The large size of nanoshell particles requires extra measures to be taken to maintain a stable dispersion of the particles in solution.

3.2 Metal Nanoshell Fabrication

Core Fabrication: Metal nanoshells are fabricated using the method developed previously by Oldenburg, et al.^{1,27} This process requires the synthesis of highly monodisperse silica nanoparticles that are used as core substrates for the electroless metallization of gold to form a thin metal shell on the core surface. Silica presents itself as an excellent core substrate for both its wide range of available sizes and facile chemical surface, but more importantly it is an optically transparent material over a broad frequency range from the visible into the infrared.

Silica nanoparticles can be made in a broad range of sizes, 10 nm – 2 μ m, using the Stöber method of particle growth and imbedded with moieties that can be made amenable to the silica growth reaction.¹⁵⁻¹⁷ These particles have a surface that is easily derivatized with a number of readily available alkoxy silane molecules. The reaction involves the base catalyzed hydrolysis and condensation of tetraethylorthosilicate (TEOS), typically TEOS and ammonium hydroxide (NH₄OH) are mixed together in varying ratios in ethanol to produce different size silica nanospheres. Typically smaller particles (80 – 250 nm) are produced for large TEOS:NH₄OH ratios, while larger particles (> 250 nm) are formed at smaller ratios. While it is possible to produce very small particles (< 80 nm) using this method, the resulting particles have irregular surface features. In this regime it is necessary to use an inverse micelle method, however, the surfactant used to prepare the micelle is difficult to remove using only centrifugation.³⁴

An important consideration in making nanoshells is the polydispersity of the starting silica spheres. The best nanoshells are fabricated on core particles with a 5 – 10 % standard deviation (% s.d.) in diameter. Particle size and % s.d. are determined by measuring at least 200 particles using a transmission electron microscope (TEM). The TEM images are evaluated using the image-processing program Image Tool. The percent standard deviation is determined as the ratio of standard deviation to mean diameter (standard deviation/mean diameter x 100). While many photonic applications, such as crystalline colloidal arrays, require particles with < 5 % s.d.,^{35,36} no significant improvement in the quality of the nanoshell solution is found by producing particles with such a small deviation in size. It has been observed that the important factor in producing a strong plasmon resonance is in the quality of the final metal shell. While a core particle with a low polydispersity is desired, exhaustive improvements to the core fabrication do not yield significant improvements to the solution quality. However, there is a notable decrease in solution quality for particles whose % s.d. increases significantly above 10 – 12 % s.d. For particles with a large % s.d. there is a significant broadening of the nanoshell spectra on the low energy side of the plasmon resonance, due to the formation of aggregates and irregularly sized particles during metal shell growth. The plasmon resonance is also significantly broadened due to inhomogeneous broadening effects that are amplified by large particle size distributions. The quality of the metal shell also decreases with large % s.d.; large size distributions decrease the range of available shell thickness that can be grown. A large range of core sizes requires a thicker shell to achieve uniform shell growth on all particles. In order to ensure a high quality, or low % s.d., core substrate it is necessary to rigorously maintain the cleanliness of the reaction

environment and reactants. However, particles with a 5 – 10 % s.d. can readily be achieved without further preparation of the reactants.

Proper preparation of the reaction vessel, typically a 50 – 200 mL Erlenmeyer flask with a ground glass stopper, requires rigorous chemical etching steps. Glassware is rigorously cleaned and then soaked in a base bath followed by an etch using a 2% HF solution. The surfaces of the glassware should be free from any visible contamination, soak times as long as 6 – 8 hours may be necessary depending on the initial cleanliness of the glassware. Care must also be taken with the purity and cleanliness of the reagents. The TEOS begins to polymerize due to moisture in the air and exposure to ambient conditions must be minimized. Both the ethanol and NH_4OH can be filtered to prevent the addition of dust or particulate matter to the Stöber reaction solution. However, at no time do the ethanol or NH_4OH require distillation. Distillation of the TEOS is necessary if particles with a better than 5 % s.d. are required.

In the case of distillation, the TEOS is vacuum distilled immediately before use. This is done using a still that allows for complete evacuation of the apparatus and also for purging with dry nitrogen. To begin, all components are washed thoroughly and soaked in base bath and HF solutions as stated in the previous paragraph. After final rinsing from the HF solution the glassware are then placed in the oven to dry (250°C for at least 30 min.). In air/moisture sensitive reactions the glassware must be in the oven to stay dry. If the glassware is allowed to cool it will become “wet” from the ambient environment and introduce impurities to the reaction. When brought out of the oven, the

reaction flasks are purged with N₂ to maintain a dry, clean environment. When distilled the TEOS begins boiling around 40° C at which time a small volume of the initial distillate is discarded before collecting the final product. This amount represents oligomers of TEOS and impurities that may be in the neat TEOS solution. The distilled TEOS is injected into the ethanol/NH₄OH solution and the reaction is allowed to proceed normally.

TEOS (mL)	NH ₄ OH (mL)	Ratio TEOS:NH ₄ OH	Ethanol (mL)	Mean Diameter (nm)	Standard Deviation (nm)	% Standard Deviation
4.5	13.2	0.34	180	171.3	11.3	6.6
4.5	14.4	0.31	180	212.7	10.5	4.9
4.5	16.0	0.28	180	242.8	12.7	5.2
4.5	16.4	0.27	180	246.2	17.5	7.1
5.1	16.0	0.32	180	240.4	16.5	6.9
4.5	20.0	0.23	180	356.1	31.2	8.8
4.5	21.6	0.21	180	391.9	24.1	6.1
4.5	21.2	0.21	180	420.7	33.3	7.9
4.5	24.0	0.19	180	465.1	29.6	6.4

Table 3.1: Table of different Stober reaction volumes. Note how particle size increases with a decrease in TEOS:NH₄OH ratio. The particles having an ~5 % s.d. resulted from distillation of the TEOS.

Surface Preparation: The next step in nanoshell fabrication involves the chemical functionalization of the silica surface with aminopropyltriethoxysilane (APTES). Once attached to the particle surface this molecule presents an amine moiety to solution, which facilitates the attachment of small gold colloid that act as nucleation sites for the electroless reduction of gold onto the particle surface. The silylation of metal oxide surfaces is a well-documented and characterized process. It has been shown that triethoxysilanes form a 5 – 10 monolayer thick interconnected network on the oxide surface.³⁷ This is due to the oligomerization of the silane bond to both the oxide surface and neighboring silane molecules. This layer presents a facile surface for the attachment of the small gold-seed colloid.

Colloidal Gold Attachment: The growth of the metal shell is facilitated by the attachment of small gold colloid to the particle surface to act as nucleation sites for electroless metallization. The gold colloid must be small in order to insure a minimum shell thickness, and be amenable to further metallization. Small gold nanoparticles 1 – 3 nm in diameter are synthesized using tetrakis(hydroxymethyl)phosphonium chloride (THPC) as the reducing agent from the method of Duff, et al.³⁸ The THPC reduced gold particles (THPC-Au) are attached to the silica particle surface and used for metal shell growth. The amount of silica particles to THPC-Au is calculated from the total surface area of the silica particle solution, the concentration and physical cross-section of the THPC-Au, and assuming 25 – 30 % coverage of THPC-Au on the silica surface.

An important consideration in the THPC-Au attachment is the amount of gold particle coverage on the silica surface. The surface coverage of an as prepared THPC-Au seed solution is limited to 25 – 30 % due to the repulsive Coloumbic interaction between the small gold particles. The gold particles have an inherent positive charge to their surface. This surface charge is offset by surface capping agents (e.g. THPC) and an electric double layer that forms around the particles as described by DLVO theory.³⁹ The electric double layer is a concentric coordination sphere made up of layers of oppositely charged ions in solution. The spatial range of the repulsive interaction between the particles is governed by the thickness of the electric double layer. Higher ionic concentrations in solution see a greater Coloumbic screening effect of this double layer. This allows the particles to come into closer contact with each other. The ionic

concentration in a solution can be described by its ionic strength ($I = 1/2 \sum_i z_i^2 c_i$). This is a function of the charge (z_i = valence) and concentration (c_i = molar concentration) of the available ions found in solution.⁴⁰

For a THPC-Au solution there are two ways that the ionic strength can be increased, thereby decreasing Coloumbic repulsion, and increasing surface coverage. The first way involves decreasing the total volume of the THPC-Au solution while maintaining the same ionic concentration. This is done by evaporating water from the solution using a rotary evaporator that takes advantage of the decreased boiling point of water under reduced pressure conditions. The ionic species do not evaporate and reducing the total volume of the solution increases the concentration. The ionic strength of a concentrated THPC-Au solution, assuming a decrease in volume by a factor of 10, is about 100 mM. This process requires careful attention to the apparatus and a controlled evacuation takes approximately 3 – 4 hours. However, this amount of preparation time can be abated by the simple addition of an inert salt to the THPC-Au solution.

A second method for increasing ionic strength involves the addition of an inert salt solution to the THPC-Au solution.⁴⁰ An aliquot of a sodium chloride (1M, NaCl) solution can be added to the THPC-Au, which introduces an adequate amount of salt to increase the ionic strength of the solution. Typically 500 μ L of a 1M NaCl solution can be added to 10 mL of a THPC-Au solution to increase the ionic strength of the solution to about 100 mM, consistent with the increase in ionic strength from rotary evaporation. Figure 3.2 shows a set of TEM images comparing the coverage of THPC-Au particles on

the silica cores when seeded from salted or evaporated solutions. It is obvious from these images that equivalent ionic concentrations yield similar THPC-Au coverage. The resulting solution can be immediately used for the seeding of silica nanoparticles. The advantage of this method is the significantly reduced preparation time. Another improvement is the ease of solution preparation when seeding the silica nanoparticles.

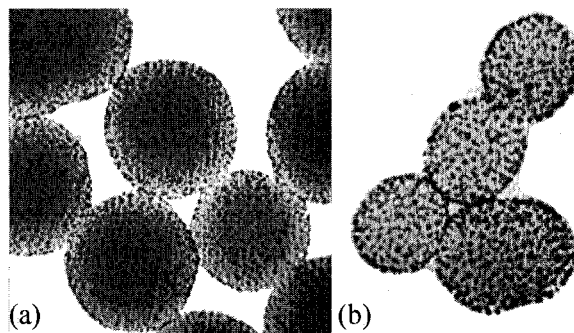


Figure 3.2: TEM images of silica cores seeded from (a) salted THPC-Au solution (116 mM) and (b) a rotary evaporated solution (95 mM)

When using rotary evaporation, a smaller volume of the THPC-Au solution is required to seed the same amount of silica particles, with respect to the original THPC-Au solution. One drawback is that this process now requires a more concentrated silica particle solution. This is due to the instability of the THPC-Au solution in ethanol. It has been observed that the seeded particle solution flocculates when the amount of the ethanolic silica particle solution is greater than half the volume of the THPC-Au solution. This requires that the silica particle solution be much smaller in volume than the THPC-Au solution when the two are mixed together. When concentrating the THPC-Au solution, this requires a more concentrated silica particle solution in order to maintain the same volume ratio as for an unconcentrated addition. The addition of a salt solution to increase

ionic strength allows for the same volume ratio of silica to THPC-Au while increasing the overall coverage on the silica surface.

Metal Shell Growth: Once prepared the seeded silica particles can be used to grow a metal shell. In order to grow a gold shell, aliquots of the seeded particles are mixed in varying ratios to an aqueous gold stock solution. Varying the ratio of seed solution volume to gold stock solution volume results in nanoshell particles with different gold shell thickness. Figure 3.3 shows a set of scanning electron microscope (SEM) images of gold nanoshells.

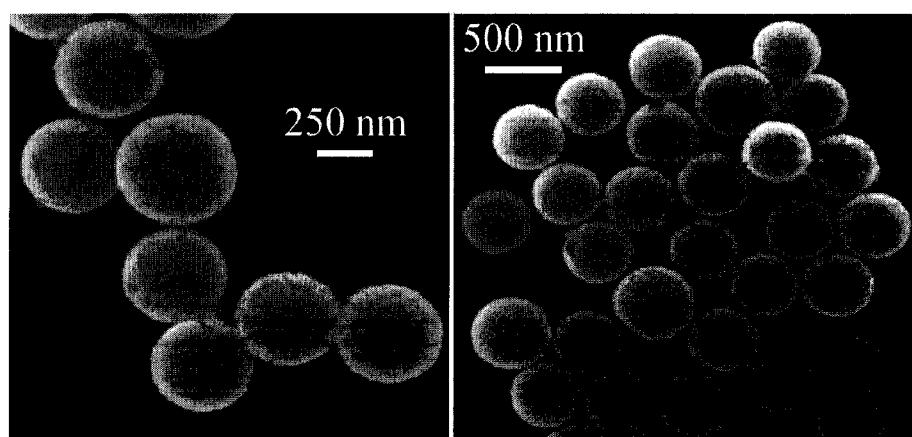


Figure 3.3: SEM images of gold nanoshells

3.3 Concentric Nanoshell Fabrication

The first step in the fabrication of a concentric nanoshell is the silica encapsulation of the nanoshells. This is accomplished using an adapted method for the silica encapsulation of small gold colloid initially described by Liz-Marzan, et al.³³ Briefly this process begins by chemically functionalizing the gold shell surface with a silane molecule followed by the condensation of a thin silica shell around the particle. This thin silica shell can then

be increased in thickness using the Stöber growth method mentioned earlier. The second metal shell is grown using standard nanoshell chemistry. Throughout the silica encapsulation step both the reactant concentration and solution pH are vital parameters to control in order to successfully encapsulate the nanoshells. This is due to the sensitive chemical nature of the species used in the growth reaction.

APTES Functionalization: One deviation from the Liz-Marzan protocol is the addition of another dialysis step before APTES functionalization. This added dialysis step was found to be necessary to produce the silica coating on the particles. Despite washing the nanoshell particle solution using centrifugation, it is necessary to remove remaining impurities in the solution, due to residual ions that remain from the stock gold solution. Negative ions coordinate and stabilize the nanoshells surface forming an electric double layer with positive ions. Other impurities such as remaining reducing agent or gold ions may also be present. Dialysis is performed using regenerated-cellulose tubing (6000 - 8000 MWCO, Spectra-Por) in a reservoir of ultra-pure (Milli-Q) water over 10 – 12 hours. More than 12 hours sees complete destabilization of the particles resulting in irreversible flocculation. Typical dialysis volumes are 30 – 40 mL of a nanoshell solution to a 4 L reservoir (1:100 volume ratio). Once the initial dialysis is done the nanoshells should be derivatized with APTES within 6 hours to avoid particle loss to flocculation. Because of the large size of nanoshell particles, they will quickly sediment out of solution over the course of the dialysis. Therefore it is also necessary to modify the dialysis process to incorporate a means of agitating the solution. Although the dialysis bag is stirring in the reservoir, this alone is not enough to maintain a stable

dispersion of nanoshells in solution. A slight modification of the dialysis apparatus includes a magnetic clamp at the bottom of the dialysis bag facing the magnetic stir bar in the reservoir. The bag is then suspended in the reservoir rather than free floating. This apparatus allows the magnetic stir bar to gently agitate the dialysis bag by alternatively pulling on each pole of the magnets on the bottom clamp. This gentle action is sufficient to keep the nanoshells suspended during the dialysis steps. It is more important to keep the nanoshells suspended during the second dialysis to allow for even and complete condensation of the silicate species.

The particles are functionalized using a dilute APTES solution at pH = 5. The APTES coordinates to the gold surface through the amine group presenting the silane group to solution. At pH = 5 this adequately charges the hydroxyl groups on the silane to maintain charge stabilization between particles and prevent aggregation. This step is also sensitive to APTES concentration. Only enough APTES to form a single monolayer on the gold surface is used, typically 30 – 20 μL (1 mM APTES, aqueous) depending on particle size. This amount is calculated from the total surface area of nanoshells in the solution and using the area occupied by the molecule on the surface (0.4 nm^2). Addition of an excess of APTES results in polymerization of the molecules and aggregation due to charge destabilization. The molecule is allowed to complex to the gold surface for 15 minutes and the particles are washed through centrifugation and redispersed in Milli-Q water. At this point a small volume of a sodium silicate solution is added. The silicate from this solution will condense onto the APTES functionalized surface to form a thin silica shell about 4 – 8 nm thick.

Thin Silica Shell Growth: The solution pH is critical at this step as too high a pH results in rapid condensation and large particle aggregates and too low a pH results in unreliable silica deposition (Figure 3.4). The silicate solution is prepared by diluting the as purchased sodium silicate (27 % wt, Na_2SiO_2 , Aldrich) in Milli-Q water to form a 0.54 % wt solution. The pH of this solution is then adjusted to between 9 and 11. This is done using chloride charged ion exchange resin (Amberlite 400A(Cl^-) IXR). The use of an IXR is required as the straight addition of an acid or buffer results in the introduction of ions that interfere in the condensation reaction. The condensation of the silicate species is readily accomplished both on the nanoshell particle and on positive ions in the solution. There is an increase in nucleation sites in the solution with the addition of excess positive ions (e.g. from an acid). This causes the formation of small silica particles in the solution rather than the formation of the thin silica shell. The use of an IXR eliminates the addition of excess positive ions. The IXR can be loaded with the appropriate ion, which is then exchanged for an ion in the silicate solution. In the case of Amberlite IXR, the resin is loaded with Cl^- from a 1N hydrochloric acid (HCl) solution. The IXR is then mixed with the diluted silicate solution and releases Cl^- . In return the IXR picks up OH^- from the silicate solution, thereby reducing the solution pH without the addition of excess positive ions, as would be the case for a straight addition of HCl. Depending on nanoshell diameter approximately 30 – 200 μL of this pH adjusted silicate solution will be added to the APTES-nanoshell solution to form the thin silica shell. The silicate concentration after addition to the particle solution should be about 0.0002 % wt. It is necessary to perform dialysis during the silicate condensation in order to prevent the

particles from growing together and the formation of residual small silica particles. By performing dialysis on the solution it is possible to regulate the condensation reaction by reducing the silicate concentration. Once the silicate is mixed with the APTES-nanoshells, the solution is immediately transferred to a dialysis bag and allowed to stir for 24 hours. This is the time necessary for the complete condensation of silica around the nanoparticles. Figure 3.4 shows a TEM image of the thin silica layer formed around a gold nanoshell. The layer is approximately 8 – 10 nm thick, but is complete and closely follows the contours of the gold shell.

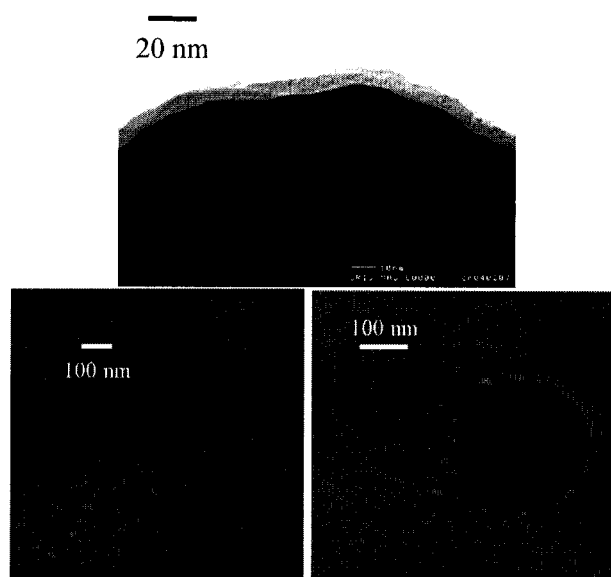


Figure 3.4: Close-up TEM image of a thin silica layer grown around a gold nanoshell (top). The silica layer is approximately 8 - 10 nm thick. The bottom images represent the results of a failed condensation reaction. The particles are surrounded by an amorphous silica network due to the self-nucleation and growth of the silicate in solution.

After 24 hours the silica encapsulated nanoshells are removed from the dialysis bag and washed using centrifugation. At this time the particles can be transferred to ethanol and the silica layer thickness increased using the Stöber reaction. The only modification to the Stöber reaction necessary for seeded growth is the dilution of the nanoparticle

solution. It is necessary to dilute a solution of large nanoshells (> 250 nm diameter) by a factor of 3 or 4, while smaller nanoshells (< 250 nm diameter) require larger dilutions by a factor of 7 to 10. The dilution is necessary to insure the seeded growth on the silica-coated nanoshells. When no dilution is done the result is multiple particles encased in a large silica network as seen in Figure 3.5(c). The dilution also helps to control the formation of residual silica particles. Some residual particle growth is expected, however, the resulting particles are typically smaller than the silica encapsulated nanoshells and can easily be separated out during centrifugation steps. A typical image of the resulting particles in this solution is shown in Figure 3.5(b). The seeded growth steps follow the same trends as the silica particle growth solutions. Therefore, larger particles require more NH_4OH than smaller particles. The amount of TEOS added determines the final silica shell thickness. This is qualitatively determined for different nanoshell batches. The silica layer can be increased controllably in 10 - 40 nm increments. Growth rates larger than 40 nm per growth cycle typically result in high concentrations of residual silica particles with similar diameters to the encapsulated nanoshells (Fig. 3.5(d)), making post-processing centrifugation difficult.

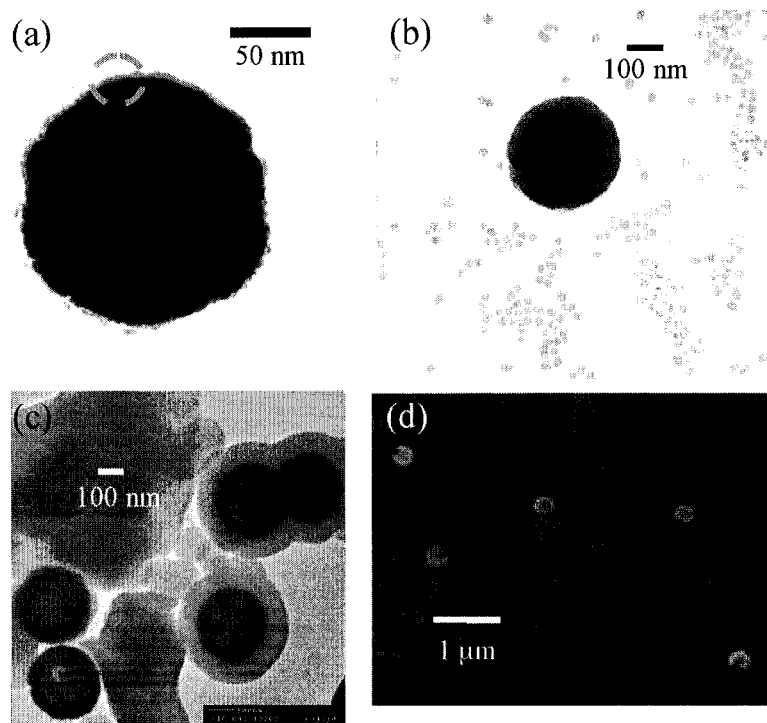


Figure 3.5: Electron microscope images of silica-encapsulated gold nanoshells. (a) TEM image of the thin silica precursor layer (b) a TEM image of a relatively thick silica shell grown under optimal conditions. (c) TEM image of the silica-encapsulated nanoshells when the solution is not diluted properly during seeded growth. Note the doublet particle and the large excess of silica. (d) SEM image of silica-encapsulated nanoshells when an excess of TEOS is added to the solution. Note the large number of similarly sized silica spheres.

Once a suitable silica shell thickness is prepared a second gold shell can be fabricated by repeating the APTES functionalization and THPC-Au attachment described earlier in this chapter. When growing the second metal shell the particle solutions need to be more dilute to account for the increased particle size. Figure 3.6 shows a series of SEM images depicting the complete process of producing a concentric nanoshell particle. Figure 3.6(a) begins with a complete gold nanoshell with an approximate diameter of 800 nm. The particle is encapsulated in a relatively thick silica shell, Figure 3.6(b), and after seeding with THPC-Au a second gold shell can be grown on the particle, Figure 3.6(c) and 3.6(d). The final concentric nanoshell particle has a diameter of about 1.4 microns.

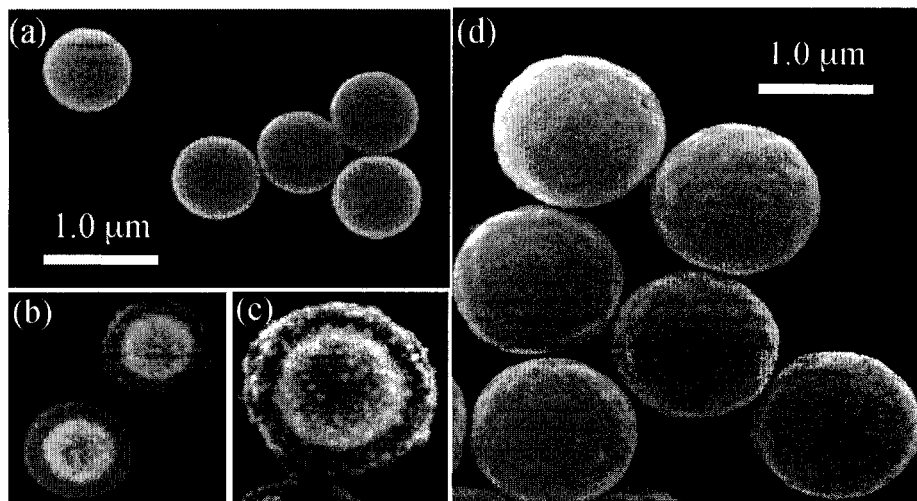


Figure 3.6: SEM images depicting the complete concentric shell fabrication process. (a) A complete gold nanoshell with an ~800 nm diameter. (b) A silica encapsulated nanoshell. (c) A silica encapsulated nanoshell decorated with THPC-Au particles (some

3.4 Reducing Agents

The importance of choosing a good reducing agent to generate a quality metal shell was investigated during the fabrication of concentric nanoshells. The necessity to generate high quality shells arose from the need to insure both a good inner shell as a platform to grow the concentric shell and both a good inner and outer shell to observe the strong plasmon coupling. Different reducing agents have been used to grow the gold shell including formaldehyde, sodium borohydride (25 mg, NaBH_4 in 20 mL water), and hydroxylamine hydrochloride (30 mg in 40 mL water).

While formaldehyde is a generally good reducing agent, it requires a longer reaction time and results in a large number of residual gold colloids forming in the solution. It has been observed that formaldehyde is a generally good reducing agent for relatively large core particles (> 250 nm) yielding a broad range of shell thickness. However, at

significantly large core sizes (> 400 nm diameter) there is an increase in the minimum shell thickness that can be grown (~ 25 nm). The gold shell on the particles in Figure 3.6(a) and 3.6(d) were grown using formaldehyde and show the difference in shell quality. While the shell in Fig. 3.6(a) is generally complete, there are fissures and cracks visible in the image. The gold shell on this particle is approximately 22 nm thick on a 792 nm diameter core. In comparison, the outer gold shell of the concentric nanoshell in Fig. 3.6(d) is about 40 nm thick and is almost defect free. Sodium borohydride reacts very quickly, but also generates a large amount of gold colloid and undergoes rapid oxidation in solution resulting in a finite lifetime to the reducing solution. Hydroxylamine hydrochloride is a generally good reducing agent similar to formaldehyde and has been observed as an optimal reducing agent for small core particles (< 200 nm). The reaction time is intermediate between the rapid reduction of NaBH_4 and the slow reduction of formaldehyde, but the generation of residual gold particles is minimized. For small core particles the range of shell thickness attainable using hydroxylamine is much wider than for the other reducing agents. This can be seen in the UV/Vis spectra shown in Figure 3.7 for nanoshells grown on a small core (~ 72 nm diameter) with the three reducing agents. What is evident in these spectra is that only the hydroxylamine reduced shells show a true tunability as the plasmon resonance first red-shifts as the shell grows, then blue-shifts with increasing shell thickness. Hydroxylamine can be used successfully on large core particles as well, but results in a smaller range of shell thickness. It has also been observed that nanoshells made with hydroxylamine appear more stable in solution and during post-processing compared with nanoshells made using

the other reducing agents. This can be ascribed to the improved stabilization of the shells from the complexation of the amine to the gold surface.

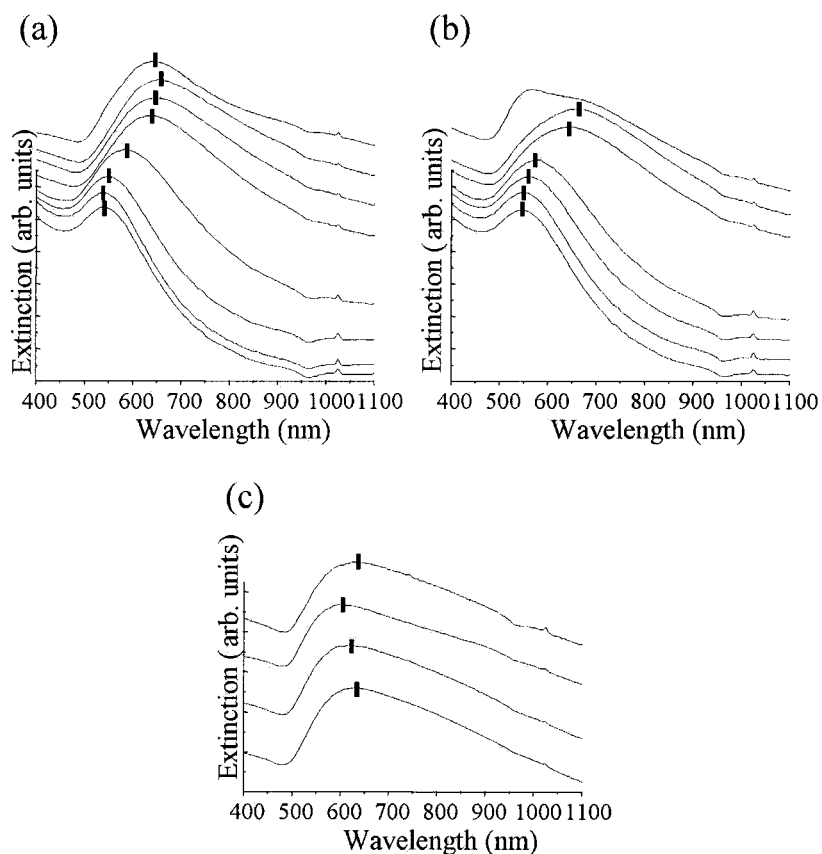


Figure 3.7: UV/Vis spectra showing gold nanoshells reduced on a 72 nm diameter core with (a) hydroxylamine hydrochloride (b) sodium borohydride and (c) formaldehyde. Note how only the hydroxylamine reduced gold shells exhibit a true tunability in the plasmon resonance.

Chapter IV: Enhanced Thermal Stability of Silica-encapsulated Metal Nanoshells

4.1 Introduction

A silica-encapsulating layer of a 60-70 nm thickness is fabricated around composite nanoparticles consisting of a silica core and a gold shell (metal nanoshells). The outer silica layer provides greatly enhanced thermal stability to the nanoparticle, effectively raising its melting temperature by 300 degrees relative to uncoated nanoshells. Both spectroscopic and microscopic structural evaluations are used to assess changes in the nanostructure when subjected to potentially destructive heating cycles. This encapsulation method may prove valuable in enhancing the thermal stability of other types of assembled nanostructures and nanoscale photonic materials.

One issue of importance with nanoshells, as with all optical materials, is thermal stability. Melting temperatures depressed below the bulk melting point of the corresponding metal are consistently observed for nanoscale metal particles.⁴¹⁻⁴⁷ In such structures, it has been observed that melting is initiated at external surfaces and along internal defects, such as grain boundaries and dislocations, and is directly affected by changes in the surface free energy of the metal.^{45,46} Metal nanoshells have an inherently high surface-to-volume ratio owing to their core-shell geometry. This results in an increased percentage of surface atoms that could be affected by surface-initiated melting, akin to a decrease in particle size for a solid metal particle. Also, the colloid-nucleated metallic shell layer may be rough and contain fissures, resulting in an increased surface area and a high number of surface defects. These characteristics accentuate the factors responsible

for melting point depression. In addition, since the metal layer will seek to minimize its free energy and segregate into a solid metal nanoparticle at elevated temperatures, any depressed melting temperature will be accompanied by a significant change in nanoshell particle morphology, and consequently, in optical response.

To counteract the inevitable temperature sensitivity of metal nanoshells, an additional nanoscale silica layer is grown around the nanostructure once metallization of the gold shell layer has been completed. Typically, silica encapsulation layers have been used to modify the solubility of nanoparticles, to control their surface charge, and to aid in biocompatibility of the resulting nanostructure.⁴⁸⁻⁵⁰ Silica layer encapsulation of metal nanoparticles has previously been reported.^{33,49,51,52} In this work, we demonstrate the fabrication of silica layers onto completed gold nanoshells. We have conducted a series of experiments on silica-encapsulated and uncoated gold nanoshells, where both their structural and optical properties are observed following heating cycles over a range of temperatures. It was observed that thick (60-70 nm) silica encapsulation layers greatly improve the thermal stability of gold nanoshells, preserving both the structural integrity of the metallic layer and the optical properties of the original nanostructure. For the silica-encapsulated nanoshells, an increase in thermal stability of more than 300 degrees Celsius, relative to uncoated nanoshells, is observed. The effectiveness of this thermally-stabilizing silica layer was observed to be dependent on its thickness: fissures that seemed to appear frequently in thinner layers appeared to compromise the encapsulation, and thus the thermal stabilizing effect of the layer.

4.2 Nanoshell Preparation

Gold nanoshells were fabricated using a multi-step process that allows for independent control over the core size and shell thickness.¹ Silica nanoparticles were made using the Stöber method.¹⁵ These particles were then functionalized with 3-aminopropyltriethoxysilane (APTES). Small gold colloid was attached to the functionalized silica particles and gold was reduced onto these seeded particles, which caused the small gold colloid to grow larger and coalesce into a shell. The gold nanoshells were modified by the growth of a silica layer on the surface of the particle, using a procedure developed initially for the encapsulation of small gold colloid described earlier.³³

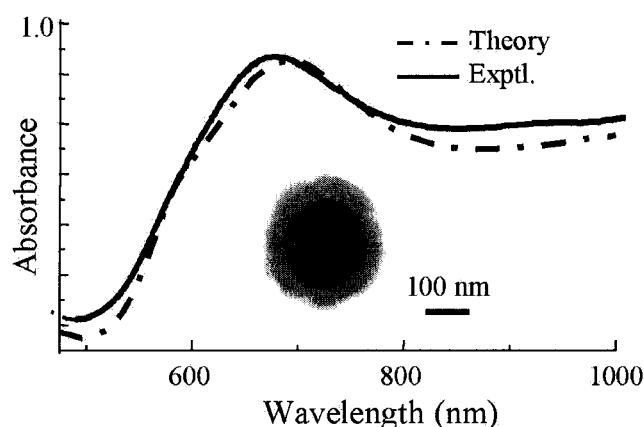


Figure 4.1: A typical absorbance spectrum for silica coated gold nanoshells. Inlaid is a TEM image of a gold nanoshell with 60 - 70 nm thick silica coating.

Figure 4.1 shows a typical absorbance spectrum for an aqueous solution of gold nanoshells coated in a thick silica layer. The spectrum is dominated by the peak at 700 nm, which, when compared to Mie scattering theory for the equivalent core-shell geometry, can be attributed to the quadrupole resonance of the metal shell.⁵³ The

absorbance shoulder, which extends from this feature to longer wavelengths in the near infrared, can be attributed to the dipole resonance of the metal shell. The dipole resonance for these core and shell dimensions occurs at 1105 nm (beyond our experimental spectral range).⁵⁴ The inset in Figure 4.1 is a transmission electron microscope image of an approximately 200 nm diameter gold nanoshell particle with a 60 – 70 nm thick silica layer.

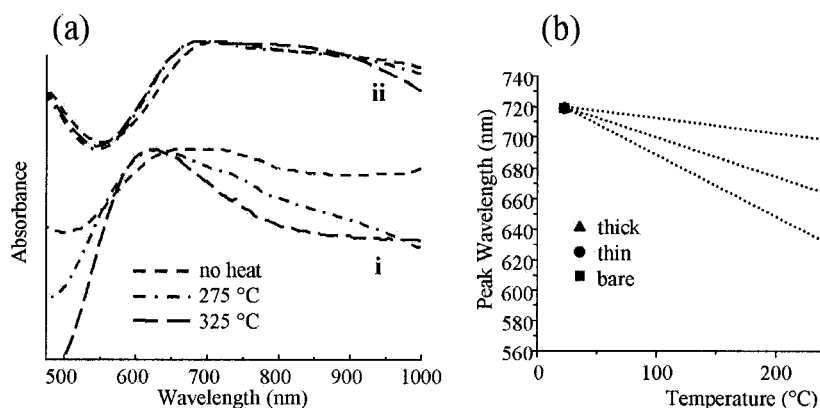


Figure 4.2: (a) Absorbance spectra for gold nanoshells with (i) a thin silica coating and (ii) a thick silica coating (b) Absorbance peak positions at each temperature.

4.3 Spectroscopic Effects of Thermal Treatment

It was experimentally determined that uncoated gold nanoshells began to melt when subjected to a 2 - 3 hour heating cycle at 275 °C and were completely destroyed following exposure to a heating cycle of 325 °C. This is significantly below the bulk gold melting temperature of 1064 °C. The gold shell was observed to melt at even lower temperatures when exposed for a longer time period, 175 °C for 12 hours. Figure 4.2(a) displays a set of nanoshell extinction spectra where the changes in absorbance following

these heating cycles are shown. Figure 4.2(a.i) shows spectra of gold nanoshells coated with a 6 - 8 nm layer of silica. Following a 3 hour heating cycle at 275 °C, the broad maximum of the nanoshell spectrum originally observed at ~720 nm has been shifted to 655 nm and is significantly narrower, suggesting that the shell nanostructure has experienced some changes in morphology. A further heating cycle to 325 °C reveals a further shift in the spectral peak of the optical response. In contrast, nanoshells encapsulated in a 60-70 nm silica layer experience only minor modifications in their optical response following heating cycles of 275 °C and 325 °C. There is an overall spectral shift of only 20 nm during the initial heating cycle, as seen in Figure 4.2(a.ii). This suggests that only minor changes in the nanoshell morphology may have occurred during this temperature cycling. In fact, the spectral shift observed in the initial heating cycle may be due to changes in the index of refraction of the thick silica encapsulant upon heating, such as H₂O elimination and further condensation of –OH dangling bonds within the silica network. Virtually no changes in this spectrum are observable between the first and second heating cycle of the sample. In Figure 4.2(b) the wavelength of the absorbance peak is plotted against temperature. The absorbance peak for bare gold nanoshells shifts approximately 100 nm when heating from room temperature to 275 °C and shifts a further 50 nm when heated to 325 °C. This change in the peak absorbance wavelength can be attributed to the melting and destruction of the gold shell.

4.4 Structural Effects of Thermal Treatment

Figure 4.3 reveals a set of scanning electron microscope (SEM) images that show the specific structural changes in nanoshell morphology for all samples, following the second

heating cycle of 325 °C. In Figure 4.3(a) the uncoated nanoshells are shown: it is clearly evident that the shell layers are destroyed following the 325 °C heating cycle. The result of melting the gold shell is the formation of large, round gold nanoparticles that no longer coat, but remain attached to, the core silica nanoparticles. This agrees with the observed changes in the extinction spectrum following both heating cycles: the final peak position for the uncoated gold nanoshells occurred at approximately 570 nm, which is typical for large gold colloid.⁵⁵

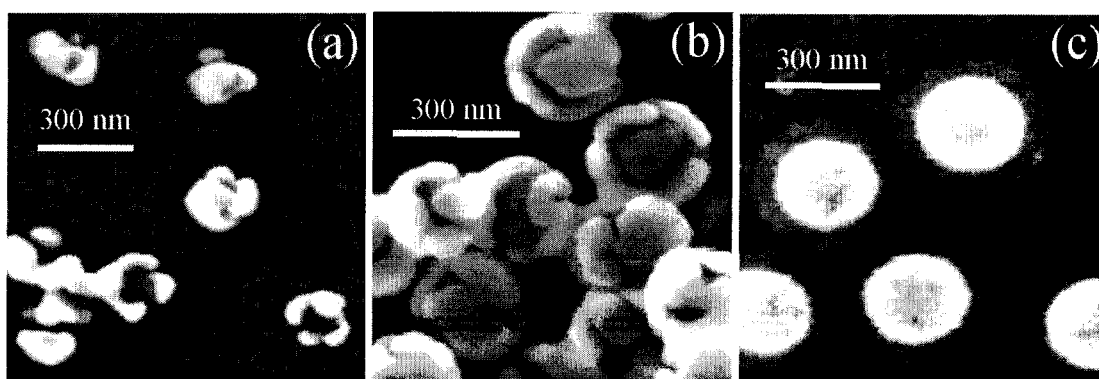


Figure 4.3: SEM images that show the effect of heating at 325 °C on shell morphology for (a) bare gold nanoshells (b) gold nanoshells with a thin silica coating and (c) gold nanoshells with a thick silica coating.

This behavior is consistent with the morphology of the gold nanoshell layer, which is formed by electroless deposition onto a colloid-coated silica nanoparticle surface. The initially formed nanoshell layer is thus composed of multiple domains, and may even exhibit fissures and cracks that are visible in TEM images of the completed shells. Since melting is initiated at defects and grain boundaries, one would conclude that multiple melting initiation sites occur, resulting in coverage of several large spherical gold clusters on the silica nanoparticle surface once the thermal cycling is complete. Figure 4.3(b) shows gold nanoshells encapsulated within a thin (6-8 nm) silica layer. These particles

have begun to melt at the visible fissures, but remain predominantly intact after being exposed to heat at 325 °C. This result suggests that the thin silica coating only exists on the gold and does not necessarily “span” the fissures. The partially increased resilience of the gold shell at elevated temperatures could then be attributed to the presence of the thin silica layer, which partially stabilizes the gold layer, preventing it from melting completely and forming gold nanospheres. Finally, in Figure 4.3(c) SEM images of gold nanoshells encapsulated with a (50 nm) thick silica layer are shown, following both heating cycles at 275 °C and 325 °C. The morphology of the gold shell is visible in the SEM image through the thick silica layer, and it appears to be unaltered following both heating cycles, indicating that there was very minimal, if any, melting of the gold shell within the silica encapsulant. From this we can draw two conclusions: the silica encapsulant can be seen to stabilize the gold shell over the range of temperatures where an uncoated shell would begin to melt, by binding to the external surfaces and features where melting could be initiated. Also, the interior silica-gold interface does not seem to have as dominant a role in initiating melting as the existence of the external surface. The surface free energy of the gold shell is decreased by the existence of the silica shell, therefore raising the melting point of the nanoscale gold shell structure. In fact, these encapsulated nanoparticles remain unaltered under heating cycles up to 600 °C.

4.5 Summary

In summary, a sufficiently thick (60-70 nm) silica encapsulation layer grown around a composite nanoparticle can greatly enhance its thermal stability relative to uncoated nanoparticles. For the case of gold nanoshells, an increase in destructive melting

temperatures of approximately 300 degrees relative to uncoated nanoshells is observed. This thermal stabilizing encapsulant layer greatly improves the robustness of metal nanoshells for optics and photonics applications, particularly in the context of high-power laser excitation, and may prove useful in the context of other nanoscale photonic materials and nanostructures.

Chapter V: Chemical Stability of Metal Nanoshells

5.1 Introduction

Nanoshells can be transferred into a range of solvents including ethanol, dimethyl sulfoxide (DMSO), THF, hexane, pentane, toluene, cyclohexane, carbon disulfide (CS_2), chloroform (CHCl_3), and carbon tetrachloride (CCl_4). Nanoshells are easily dispersed in polar organic solvents, particularly ethanol and DMSO. In order to facilitate the transfer of the nanoshells into non-polar organic solvents it is necessary to functionalize the particle surface with a molecule suitable to a non-polar environment. This is easily achieved by using the well-known affinity of thiols for gold surfaces. Owing to the large number of thiols available, there are an ample number of suitable molecules that can be attached to the nanoshell surface allowing the particles to be transferred into non-polar solvents. Despite the ease of transfer into non-polar solvents it has also been observed that nanoshells are unstable in some of these solvents over long-term exposure times, particularly true of the halo-alkanes CHCl_3 and CCl_4 . A surprising chemical reactivity of gold nanoshells was observed with carbon tetrachloride and chloroform. Evidence is shown for the decomposition of the gold shell due to a reaction with carbon tetrachloride. The reaction is believed to proceed through the formation of a charge transfer complex between carbon tetrachloride and the gold-amine complex. The reaction is facilitated by the presence of defects in the shell layer.

The decomposition of gold nanoshells in carbon tetrachloride (CCl_4) was observed during the development of multi-layer, concentric sphere nanoshell particle consisting of four

concentric, alternating layers of dielectric and metal. These specific particles have a silica-gold-silica-gold composition in concentric sphere geometry. The interest in these particles lies in the enhanced infrared extinction properties due to the presence of the outer gold shell. In order to characterize a particle with infrared extinction using standard spectroscopic methods, it is typically necessary to transfer the particles into a solvent or medium that is highly transparent across the spectral region of interest. Carbon tetrachloride is a particularly attractive solvent due to its wide optically transparent transmission range across the infrared. We report here the observation that prolonged suspension of nanoshells and nanoshell-based layered nanoparticles in CCl_4 results in the chemical decomposition of the layered nanoshell structures.

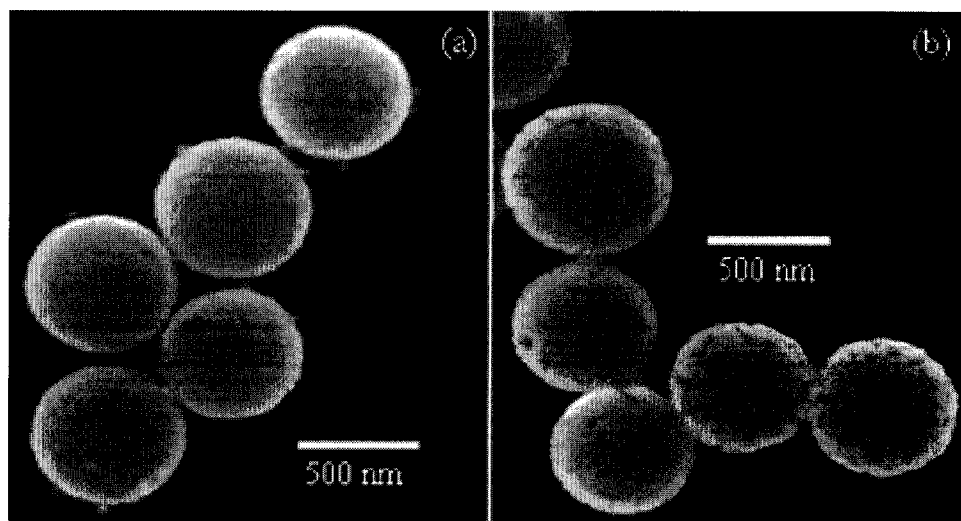


Figure 5.1: Typical gold nanoshells that can be fabricated with (a) almost defect free gold shells, (b) multiple defect gold shells

5.2 Nanoshell Preparation

Gold nanoshells were fabricated using the previously described method. Once prepared, the nanoshells were processed to remove excess reactants using centrifugation. Figure

5.1 shows typical nanoshell particles prepared using this method. The particles depicted in Fig. 5.1(a) are complete nanoshells with few defects in the shell structure, while the particles shown in Fig. 5.1(b) have multiple defects visible in the shell structure. It is important to note that both types of nanoshells (Fig. 5.1(a), 5.1(b)) have a strong optical signature with multipole components to the plasmon resonance.

In order to facilitate the transfer of gold nanoshells into carbon tetrachloride (CCl_4) it is necessary to derivatize the gold surface with an alkanethiol. We prepared a 2 - 20 mM solution of dodecanethiol ($\text{C}_{12}\text{H}_{26}\text{SH}$) in ethanol. The nanoshell particles were centrifuged and redispersed in ethanol at a concentration of $1 \times 10^9 - 1 \times 10^{10}$ particles/mL, an aliquot of the thiol solution was mixed to an equal volume of the nanoshell particle solution. The particles were stirred and allowed to sit overnight in order to ensure complete attachment of the thiol to the gold surface. The dodecanethiol-derivatized nanoshells were then centrifuged and redispersed in CCl_4 .⁵⁶

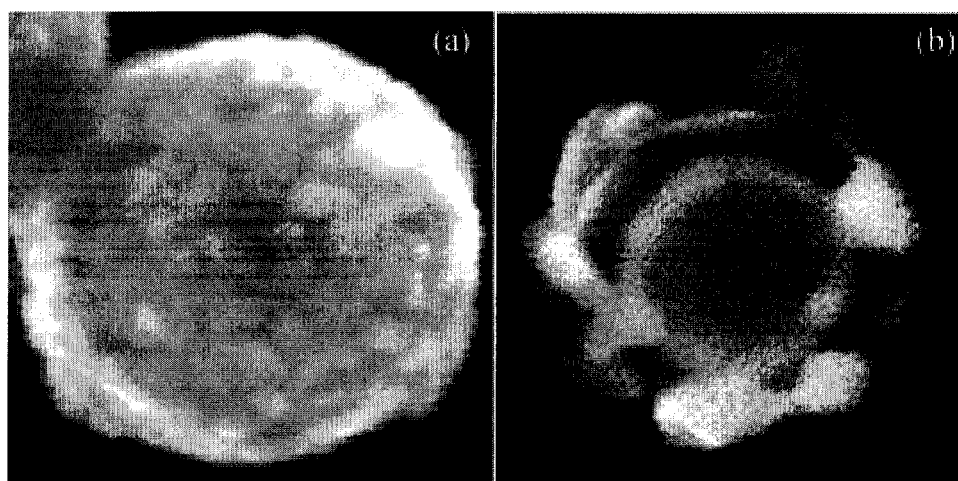


Figure 5.2: Concentric sphere nanoshell particle (a) before and (b) after dispersal in CCl_4 .

Particles were characterized using a Philips XL-30 environmental scanning electron microscope (ESEM) to determine particle size and gold shell structure. Optical characterization of the particles was performed using a Hitachi U-2001 UV/Vis spectrometer.

5.3 Gold Shell Decomposition in CCl_4

The first observation of gold shell decomposition in CCl_4 was during the development of the four-layer, concentric nanoshell. Figure 5.2(a) is an SEM image of such a particle. The outer gold shell is rough, consisting of bound gold colloid that is beginning to coalesce after gold ion reduction. The solution of concentric sphere particles was derivatized with 1-dodecanethiol in order to transfer the particles from ethanol into CCl_4 . Upon transfer to CCl_4 the particles appeared to degrade over a period of a few hours (< 5 hours). This was easily observed by eye, as a visible change in the color of the suspension that began to appear gray, followed by rapid particle flocculation. An SEM image depicting the state of the concentric sphere particles after decomposition in CCl_4 is shown in Figure 5.2(b). In order to investigate this phenomenon, two layer nanoshells consisting only of a silica core and a gold shell were fabricated, derivatized with dodecanethiol, and transferred to CCl_4 . The single gold nanoshell particles are shown in Figure 5.3(a). The solid line in Figure 5.3(c) is an extinction spectrum for these particles. The multipole plasmon resonances are evident: the dipole peak at 1000 nm and the quadrupole peak at 700 nm can readily be distinguished. These particles are representative of typical nanoshells produced by the fabrication method. These particles have a deep green color when they are in an aqueous suspension. The particles visible in

this picture are complete shells, but they possess some cracks and fissures in the shell structure characteristic of the shell growth process. The shell grows by reduction of gold ions onto a silica particle surface that is decorated with small gold colloid. As the small particles grow and begin to coalesce there can be cracks and fissures where the gold does not grow together evenly. This is more typical for gold shells that are relatively thin (< 15 nm), whereas relatively thick gold shells (15 – 30 nm) are complete possessing fewer defects. From observations it has been determined that the transition from a thin to thick shell is relative to the core diameter of the particle and typically follows the development of a strong quadrupole resonance in the extinction spectrum.

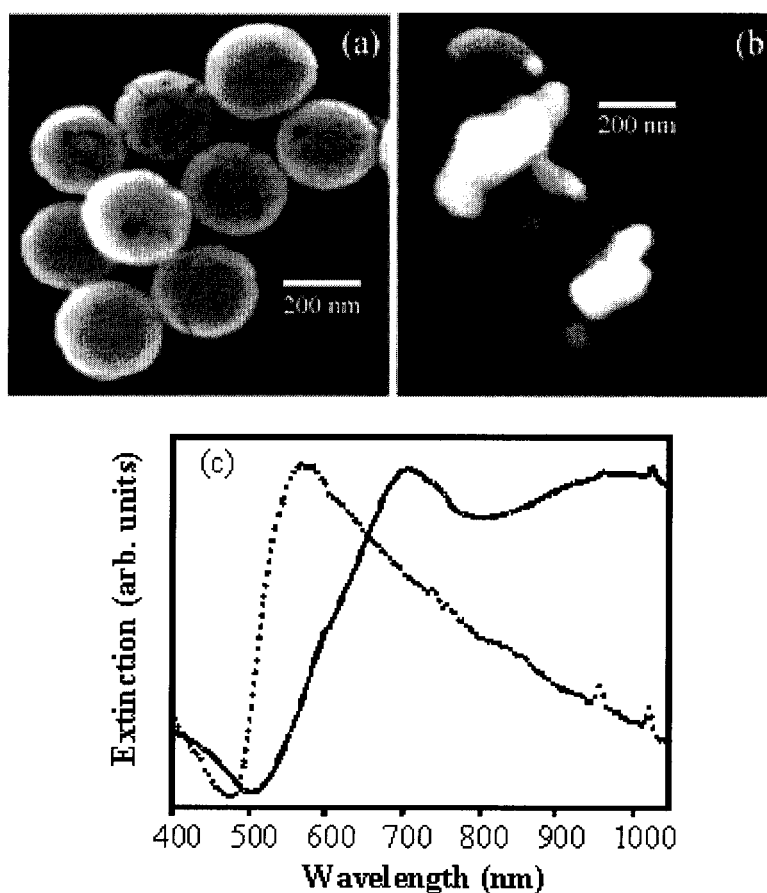


Figure 5.3: Gold nanoshell particles (a) before and (b) after dispersal in CCl_4 . (c) The extinction spectra for complete (solid line) and decomposed (dashed line) nanoshell particles.

The particles in Figure 5.3(a) were derivatized with 1-dodecanethiol and transferred to CCl_4 . The particles were suspended in the solvent for approximately 12 hours. After this time the color of the suspension had changed from green to red. The SEM image in Figure 5.3(b) shows the state of the nanoshell particles after suspension in CCl_4 . Here it is apparent that the gold shell has decomposed and formed large gold colloid, a fact consistent with the observed color change of the suspension. A mixture of large (> 100 nm) and small (< 100 nm) gold particles is observable. This would correspond with the decomposition of different size plates of gold formed during the shell growth process. The number and dimensions of the cracks in the gold shell would determine the size and nature of these gold particles. The dashed line in Figure 5.3(c) is the spectrum of this decomposed solution. The spectrum has evolved into a single, large peak located at approximately 575 nm, corresponding to a typical spectrum for large gold colloid. The broad peak and long tail into the near infrared coincide with a dispersion of different gold particle sizes.⁵⁵

5.4 Effect of Solvent and Shell Structure on Decomposition

In order to verify that CCl_4 was indeed reacting with the gold shell, the fabricated particles were dispersed in a variety of different organic solvents. The dodecanethiol-derivatized gold nanoshells were dispersed in chloroform (CHCl_3), carbon disulfide (CS_2), pentane (C_5H_{12}), and toluene (C_7H_8). None of these solvents caused decomposition of the gold shell. Another factor to investigate is the shell structure. In order for the CCl_4 to react with and remove the gold shell from the silica particle surface it would be necessary for the CCl_4 to diffuse through the shell to the APTES-gold

interface. This would be facilitated by the defects sometimes found in the shell. An increase in the number and size of the defects would result in a more rapid degradation of the shell. Gold nanoshell particles similar to those shown in Figure 5.1(a) having almost no defects in the shell are stable in CCl_4 for an indefinite period of time. No change in the structure or extinction spectrum was observed in near defect-free nanoshells over a period of 5 days. Particles were then fabricated with a high number of defects by purposely growing an incomplete shell. These particles are depicted in Figure 5.4(a). The shells are incomplete and consist of large gold colloid that had not coalesced to form a solid shell. When a solution of these particles was dispersed in CCl_4 , there was a rapid degradation (< 5 hours) of the shell relative to the degradation of gold nanoshells with a low defect density. It is clear from Figure 5.4(b) that the large gold particles have been stripped from the silica nanoparticle surface. This same test was performed on gold-decorated silica particles. However, the nature of the small seed gold is such that any change to a non-aqueous solvent results in the aggregation of the gold particles on the silica particle surface.

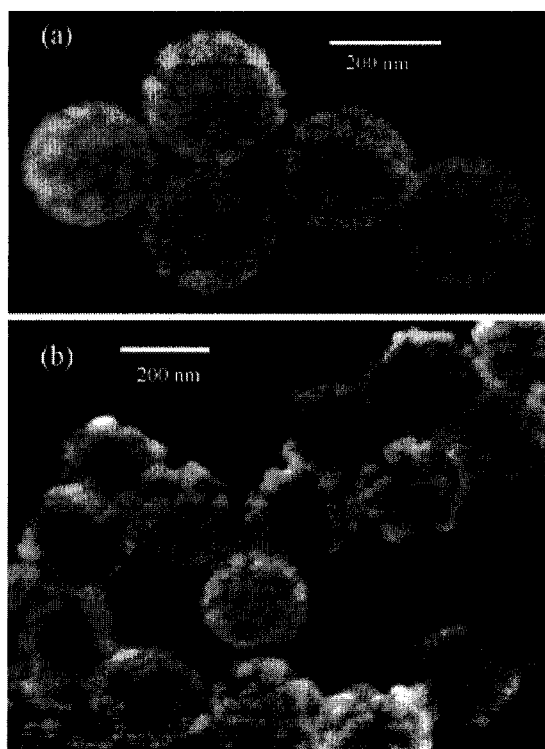


Figure 5.4: Incomplete nanoshell particles (a) before and (b) after dispersal in CCl_4 .

5.5 Reaction of Primary Amines with CCl_4

One explanation for the decomposition of the gold nanoshell when dispersed in CCl_4 is a reaction between the CCl_4 molecule and the amine moiety used to derivatize the silica surface. The reaction between primary amines and CCl_4 has been studied in different environments and can be initiated by UV light, O_2 , and by transition metals or their salts.⁵⁷⁻⁶⁰ These reactions occur under mild conditions and are typically facilitated by a charge transfer complex. The products of these reactions include trichloromethyl radicals, chlorinated amines, metal chloride salts, and chloroform. Therefore, the CCl_4 molecule can react at the gold-amine interface. The resulting gold-amine- CCl_4 complex will dissolve, separating from the gold shell. Since the amine is anchored to the silica particle, the result is a separation of the gold shell at the reaction point. The formation of

the amine- CCl_4 complex at the attachment point of the gold shell destabilizes the shell structure. Once the reaction occurs the shell can be released into the solution. If the shell has a large number of defects then this process can proceed relatively quickly resulting in the complete decomposition of the gold shell. The trichloromethyl radicals are then available to react in solution with any of the other products. This may result in the reduction of gold ions found in the form of gold chloride, a possible by-product of the initial reaction, or the reaction between gold particles released from the silica particle surface.^{61,62} This may explain the presence of larger gold particles shown in Figures 5.2(b) and 5.3(b).

5.6 Characterization of Amine- CCl_4 Reaction

Previous studies of amine- CCl_4 reactions have used UV, infrared, and Raman spectroscopy to characterize the charge transfer complex and the reaction products.^{57-60,63} It was not possible to reasonably employ these techniques in this work due to the nature of the nanoparticle system. The charge transfer complex formed between the amine and CCl_4 can be observed in the UV region of the spectrum. However, with gold nanoparticles and nanoshells, there is a large extinction value in the UV spectrum due to the interband transitions that occur in the metal. These transitions are highly absorbing in the region around 300 nm where the charge transfer complex can be observed. If the reaction proceeds through the formation of a gold-amine- CCl_4 complex, then there will be a relatively small concentration of these sites making it difficult to isolate the reaction products. This makes infrared spectroscopy a difficult measure of the process. Raman spectroscopy can be used to observe changes in the structure of CCl_4 . However, because

CCl_4 is both the reactant and the solvent it is impossible to observe a change to the small fraction of CCl_4 molecules that will react.

5.7 Conclusions

We have observed a surprising reactivity of gold nanoshells with CCl_4 , which results in the decomposition of the metallic shell layer of the nanoparticle under prolonged suspension in CCl_4 . The observed decomposition appears to be due to the formation of a charge transfer complex involving CCl_4 at the amine-gold interface. This complex results in the dissolution of the amine-gold linkage, releasing gold shell fragments into suspension. This process was observed when different types of nanoshell particles were dispersed in CCl_4 . Images obtained using SEM show the decomposition of the shell into large irregularly shaped gold colloid, which coincides with the extinction spectra of the particles showing the evolution of the nanoshell extinction into that of large gold colloid. The surprising reactivity between CCl_4 and nanoshells is potentially quite technologically important since it would be generally characteristic of the colloid-seeded metallization chemistry of nanoshells, which may more generally be applied to a broader range of nanostructures and nanopatterned surfaces.

Chapter VI: Optical Properties of Concentric Nanoshells

6.1 Introduction

Concentric nanoshells are nano- or microparticles with a concentric sphere geometry having multiple nanoscale layers of controlled thickness. A concentric nanoshell with a dielectric-metal-dielectric-metal structure supports plasmon resonances that can be tuned across the infrared region of the electromagnetic spectrum by varying the thickness of the particle's constituent layers. The nature of the concentric nanoshell plasmon resonance can be explained using the sphere-cavity model of plasmon hybridization. Experimentally observed optical extinction of the particles agrees quantitatively with Mie scattering theory for the concentric sphere nanostructure.

The area of nanoparticle research has seen the continued evolution of different particle morphologies offering unique physical and optical properties owing to specific nanoparticle materials and geometries. In the area of metallic and semiconductor nanoparticles, different synthetic routes have been developed to create unique particle geometries with optical properties differing from that of the spherical colloid.^{1,2,64-78} While the gold colloid plasmon resonance can be moved over a small wavelength range simply by increasing the colloid diameter, typical growth strategies result in a particle size population with a large deviation in particle sizes. Recently, Murphy and co-workers have shown that a controllable seeded growth of gold colloid is possible without sacrificing low dispersity in colloid size.^{79,80} Even with this technique, the plasmon resonance is limited to a small wavelength range. Gold nanorods have been shown to

have an improved size tunable plasmon resonance. Gold nanorods possess two plasmon resonances associated with the longitudinal and radial dimensions of the rod. The longitudinal plasmon resonance can be tuned across the near infrared region of the spectrum. Different groups have demonstrated the tunability of the longitudinal plasmon resonance by increasing the overall length of the nanorod.^{2,71,81,82} Semiconductor quantum dots are another class of nanoparticle that possess a size tunable optical absorption. Typically this absorption occurs at visible wavelengths, but lead sulfide (PbS) quantum dots have been fabricated which possess a near infrared exciton absorption.^{83,84} Alivisatos and co-workers have fabricated semiconductor nanorods of cadmium selenide (CdSe) that possess a tunable exciton absorption associated with the longitudinal nanorod axis.⁶⁹ Increasing the nanorod length tunes the absorption into the near infrared. Unfortunately for semiconductor quantum dots the size tunability is typically over a small spectral range limited by the small size regime of the nanocrystallite material. Theoretically a continued increase of the rod aspect ratio should tune the absorption of the metal or semiconductor particles across the infrared spectral range. This approach is dependent on what particle dimensions are feasible using current synthetic routes and the stability of these particles in different environments.

The optical response of metal nanoshells is determined by their plasmon resonance, which is a sensitive function of the particle core diameter and shell thickness (Chapter 2). For particles with a silica core and a gold shell, the plasmon-derived optical extinction has been tuned across most of the visible region of the spectrum and into the infrared, from nominally 650 nm to 2.2 μm .⁵⁴ The current synthetic route, described in Chapter 3,

is limited to a minimum core size of approximately 80 nm. This limits the tunability of gold nanoshells to be within the visible-to-NIR region of the spectrum. For gold nanoshells this prevents particles being made with a plasmon resonance across the entire visible spectrum. Utilizing a silver shell, which has a plasmon resonance tunable over a greater range in the visible, can offset this.⁷⁰ The highly frequency-agile optical response is unique to metal nanoshells, and promises potential applicability in a broad range of technologies.

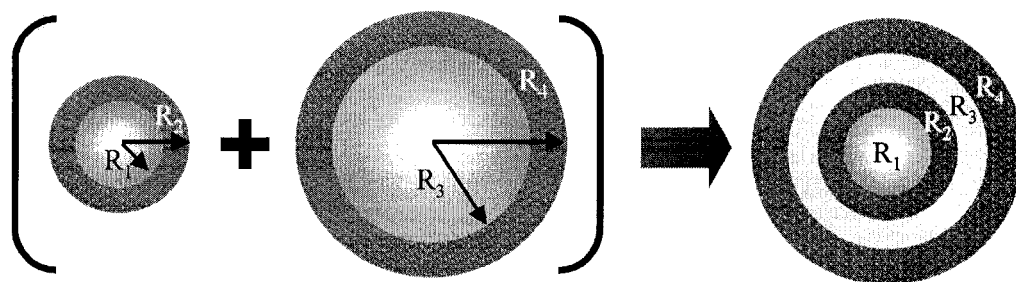


Figure 6.1: Schematic illustrating the concept of the concentric nanoshell particle. The concentric nanoshell is constructed by embedding a smaller nanoshell in the core of a larger nanoshell. The layers of the particles are labeled by their radii.

The size tunability of nanoshells must also be investigated for a regime that can easily tune the plasmon resonance through the infrared region. Simply increasing the core:shell ratio should result in unlimited tunability across the entire electromagnetic spectrum. To date, nanoshells have been prepared that can span the visible and near infrared regions of the spectrum. The motivation for this work was to determine a suitable particle geometry that would result in a plasmon tunable across the mid infrared region of the spectrum. This could prove beneficial for applications such as surface enhanced infrared absorption spectroscopy (SEIRA) or enhanced thermal conductivity.¹² While the current core synthesis can produce particles in excess of one micron in diameter, it is unknown if the

current shell synthetic procedure will reach a limit for growth on larger core particles. To this end we have investigated a change in the morphology of the nanoshell particle in order to expand its optical range. By encapsulating a metal nanoshell with a dielectric layer it is possible to grow a second metal shell and create a four layer, concentric sphere particle that has a dielectric-metal-dielectric-metal geometry. Figure 6.1 is a schematic of the multi-layer particle. Specifically we have created a particle with a silica-gold-silica-gold composition that has a strong infrared plasmon resonance that extends into the mid infrared region of the spectrum.

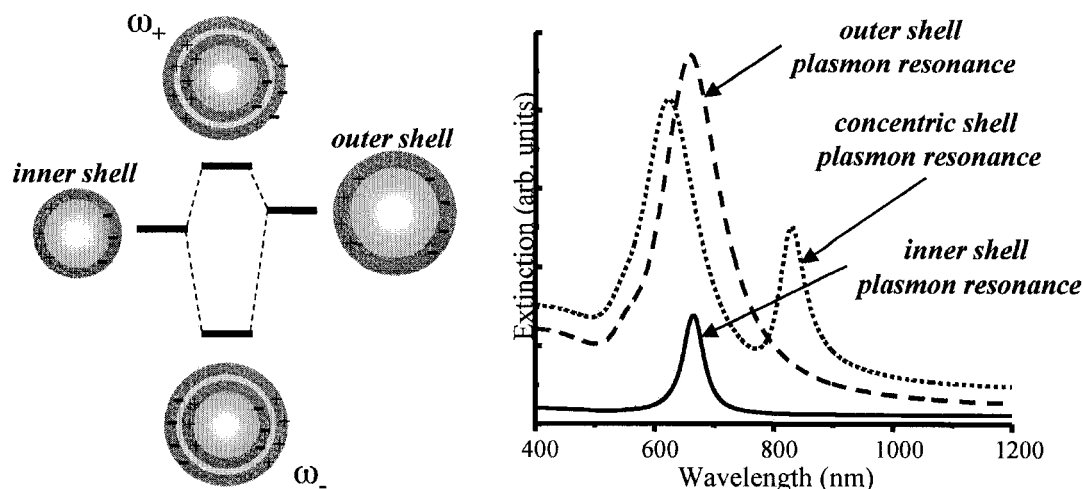


Figure 6.2: Simplified energy level diagram of the plasmon hybridization in a concentric nanoshell due to the plasmon coupling between the symmetric polarizations of the single shell plasmons (a). Set of calculated extinction spectra for different nanoshell particles.

Typically, silica encapsulation layers have been used to modify the solubility of nanoparticles,⁵² to control their surface charge,⁶⁸ to aid in biocompatibility of the resulting nanostructure,⁸⁵ to act as a thermally resistant coating,⁸⁶ and to aid in the formation of crystalline arrays. The silica encapsulation of a gold nanoshell, as described in Chapter 3, provides a layer that is chemically invariant from the silica core material.

This allows for the application of the nanoshell synthesis to the silica encapsulation layer in order to grow a second metal shell. The resulting multi-layer particles match Mie scattering theory quantitatively. In comparing the experimentally measured absorption spectra with Mie scattering theory it is evident that by moving to a multi-layer configuration this distinct particle geometry allows for an increase in the infrared spectral range of the nanoshell particle. Furthermore, it is apparent that there is a regime where the spectral range of the particle plasmon resonance is unaffected by the multi-layer configuration. This opens interesting questions about the nature of the nanocavity created by the nanoshell geometry.⁸⁷

The optical response of the concentric nanoshell particle can be described using the sphere-cavity model introduced in Chapter 2. The energy level diagram for the concentric shell system is depicted in Figure 6.2. For clarity the diagram is simplified and assumes hybridization for only the interaction between the symmetric coupling modes of the single-layer nanoshell plasmons. Using this model the plasmon resonance is described as the hybridization of the energy levels of the two single-layer nanoshell plasmons arising from the inner and outer metal shells. The hybrid plasmon is dependent on the plasmon coupling strength, which is a function of the particle's core-shell dimensions.

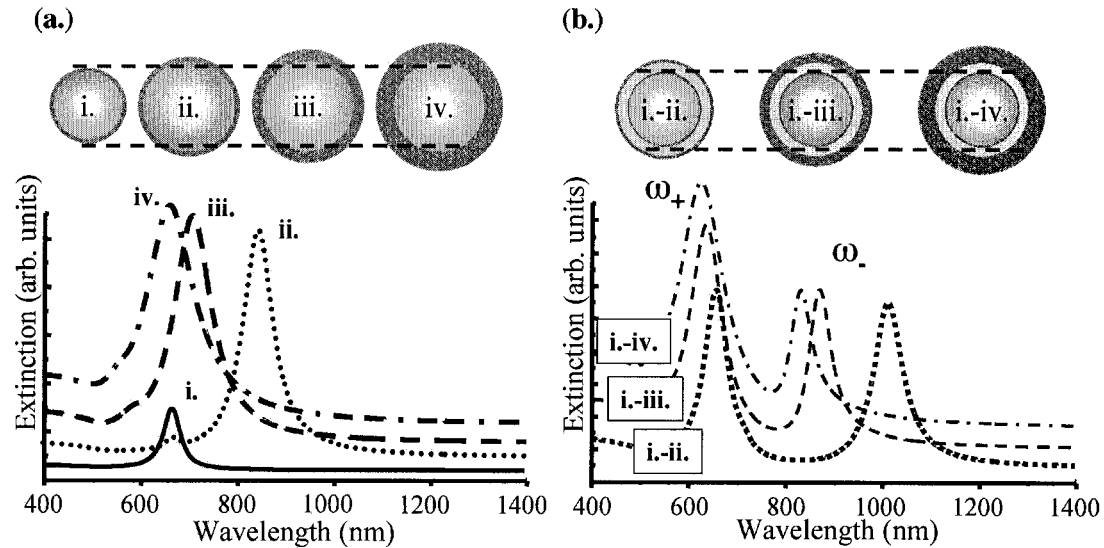


Figure 6.3: Theoretical calculations showing (a) the single-layer nanoshell response for different nanoshell particles and (b) the plasmon response for a series of concentric nanoshell particles constructed from the single-layer nanoshells shown on the left.

6.2 Mie Scattering Theory for a Concentric Nanoshell

Using Mie scattering theory (Chapter 2) to model the multi-layer system it was found that the multi-layer dielectric-metal-dielectric-metal configuration would increase the spectral range of nanoshell particles. An example of these calculations is shown in Figure 6.3. The calculations shown in this figure are carried out using the Johnson and Christy derived dielectric function and excluding broadening due to electron scattering from the shell. This figure demonstrates the increased spectral range of the multi-layer particle over that of the single shell particles. The concentric nanoshell particles in Fig. 6.3(b) have two peaks associated with the hybridized plasmon. It is important to note that the multi-layer nanoshell spectrum is not simply the superposition of the inner and the outer single layer nanoshell spectra. Rather, the plasmon resonance of the concentric nanoshell is due to the hybridization of the inner and outer metal shell plasmons. The peaks in the

concentric nanoshell extinction are due to the symmetric and anti-symmetric eigenmodes that arise from the hybridization scheme. The calculations show the response of the different modes of the hybridized plasmon to changes in the outer shell thickness (R_4) while holding the inner particle dimensions (R_1 , R_2 , R_3) constant. The high energy, anti-symmetric (ω_+), mode is found between 600 and 650 nm. There is relatively little shift in the location of this mode with respect to changes in the particle geometry. However, the low energy, symmetric (ω_-), significantly changes position with variation in the outer shell thickness and is shifted between 150 to 200 nm with respect to the single shell plasmon resonances.

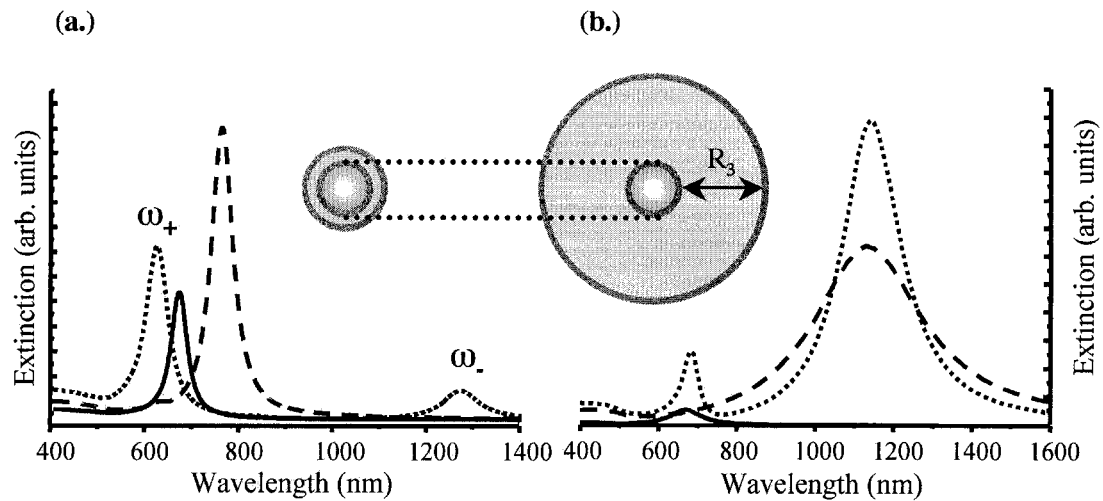


Figure 6.4: Theoretical calculations depicting (a) the strong coupling regime for a concentric nanoshell with a small R_3 and (b) a regime where the two shells are decoupled owing to a large R_3 , resulting in no plasmon hybridization.

The plasmon resonance of the concentric nanoshell is also dependent on the interaction distance between the two metal shells. The magnitude of the separation between the two shells determines the strength of the plasmon coupling resulting in the hybrid plasmon. Figure 6.4 shows the dependence of the concentric nanoshell hybridization on interaction

distance. The spectra are calculated using the same parameters as for Fig. 6.3. The particle geometry on the left depicts a strong coupling regime where the inner and outer shells are in close proximity. This results in a strong plasmon-plasmon interaction, which is reflected in the strong splitting of the concentric nanoshell plasmon. The two modes of the hybrid plasmon are clearly seen. For the particle on the right, which has a large R_3 separation distance, the two metal shells are decoupled and the concentric nanoshell plasmon is merely the superposition of the two single-layer nanoshell plasmon modes.

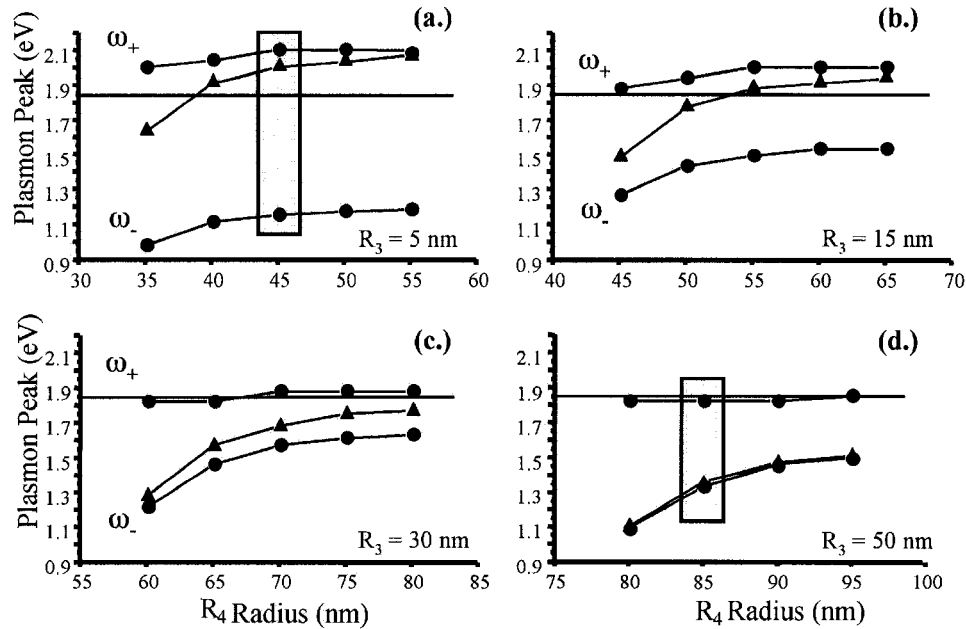


Figure 6.5: Summary of theoretical calculations of the plasmon peak position exhibiting the trends in plasmon hybridization when changing concentric shell dimensions. In each part the outer shell thickness (R_4) is varied with respect to constant inner shell dimensions (R_1 , R_2 , R_3), the separation distance is increased going from (a) to (d). The peak position of the hybrid (circle), inner (solid line) and outer (triangles) plasmon modes are plotted vs. outer shell thickness (R_4). The hybrid modes (ω_+ , ω_-) are labeled for clarity in (a) to (c). There are no hybrid labels in (d) as the shells are decoupled.

Figure 6.5 shows the general trend in plasmon hybridization for different particle dimensions in the concentric nanoshell particle. In each part of Fig. 6.4 the outer shell thickness, R_4 , is tuned with respect to constant inner particle dimensions (R_1 , R_2 , R_3), while the separation layer, R_3 , is changed from 5, 15, 30, to 50 nm going from Fig. 6.5(a)

to 6.5(d), respectively. It is evident from these calculations that tuning the core-shell ratio of the outer metal shell controls the peak position of the hybrid plasmon modes. By tuning the core-shell ratio of the outer shell the hybrid plasmon modes can be tuned in energy, whereas tuning the separation distance between the inner and outer shells controls the strength of the plasmon interaction. This can be seen from the relatively strong coupling regime of the 5 nm separation in Fig. 6.5(a) compared to the complete decoupling of the inner and outer shells seen in Fig. 6.5(d) where there is no hybridization of the concentric nanoshell plasmon.

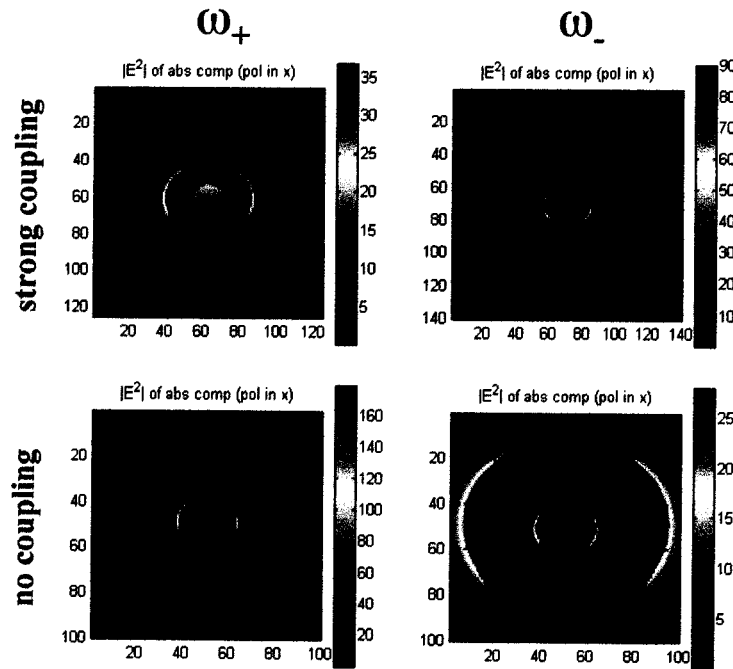


Figure 6.6: Near-field maps for concentric nanoshells taken as a slice through the particle. The particle dimensions are the same for the highlighted particles in Figure 6.4 to show the difference in field strength for the strong and no coupling regimes. The light is incident on the particle from the bottom of the plot with the electric field polarized in the plane of the paper.

The intensity of the near-field, taken as a slice through the particles, around two different concentric nanoshell particles is shown in Figure 6.6. The particles used to calculate

these near-field maps have the same dimensions as the highlighted particles in Fig. 6.5(a) and 6.5(d). Figure 6.6 illustrates the difference in the interaction distance between the inner and outer shell and the effect on plasmon hybridization. In the strong coupling regime the small separation distance between the inner and outer shell results in a strong interaction of the near-fields generated by the plasmons of the inner and outer shell. An interesting trend is also apparent from Fig. 6.5, in that the symmetric hybridization mode of the concentric nanoshell particle is red-shifted with respect to the inner shell plasmon at larger overall particle sizes (Fig. 6.5(c) and 6.5(d)).

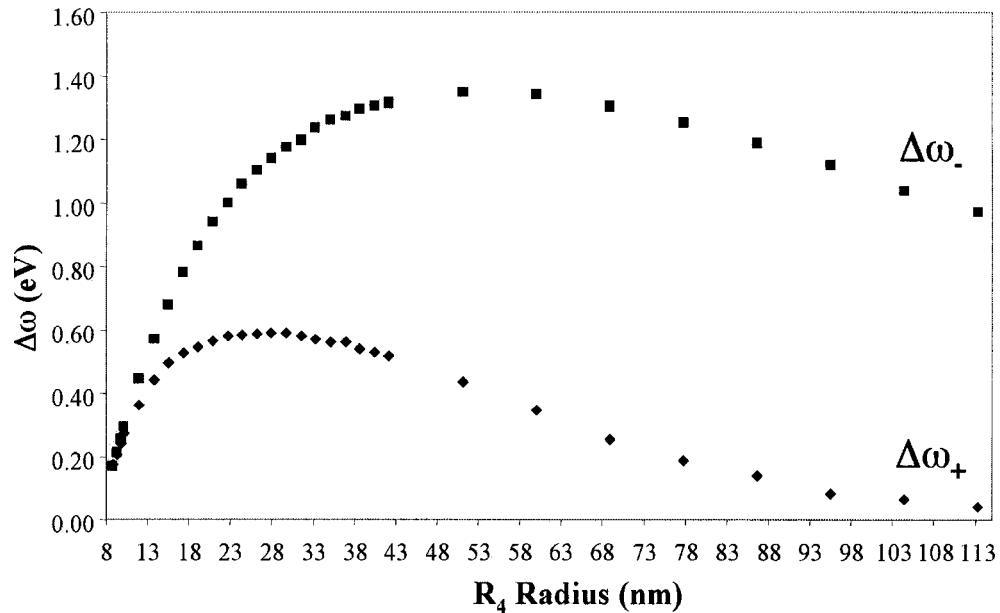


Figure 6.7: Graph of the difference in peak position ($\Delta\omega$) between the symmetric (ω_+ , diamonds) and anti-symmetric (ω_- , squares) modes of the concentric nanoshell plasmon with respect to the single-layer nanoshell plasmon. In these calculations core-shell ratio was held constant at 0.75 while total particle radius (R_4) was increased by $\sim 5\%$ increments. A Drude dielectric function was employed to exclude the effects of core electrons and all broadening mechanisms were neglected in order to accurately determine peak position.

In trying to explain this trend in the calculations, it was found that a significant contribution from the d-electrons in the metal was affecting the hybrid modes of the

concentric shell. The d-electrons of the metal ion cores contribute to the polarizability of the positive background of the metal in the Drude model. This background dielectric will red-shift the energies of the plasmon modes. The effect of this contribution is strongest on the cavity plasmon in the nanoshell system. In the concentric nanoshell system, the inner shell mode is analogous to the cavity mode. Therefore, the red-shift observed in Fig. 6.4 for the symmetric mode of the concentric nanoshell plasmon can be explained in terms of this d-electron contribution. Figure 6.7 is a presentation of the calculations made to investigate the effect of the d-electrons on plasmon hybridization. The difference in the peak position of the hybrid plasmon modes, $\Delta\omega$, with respect to the single nanoshell modes is plotted against total particle radius, R_t . In these calculations a Drude dielectric function for gold was employed neglecting the high frequency contribution (ϵ^∞ , Chapter 2) in order to exclude the d-electron effects. What is evident from Fig. 6.7 is that in the dipole limit for small particles the splitting between the ω_+ and ω_- modes is symmetric about the single-layer nanoshell plasmon mode. The hybridization deviates from this symmetric behavior as the particles move beyond the dipole limit. This is due to phase retardation effects resulting in the evolution of the higher order multipole resonances. In the dipole limit at constant core-shell ratio, the plasmon modes for the inner and outer shell are “in tune”, that is they are found at the same frequency. However, with the introduction of higher order multipoles, this red-shifts the plasmon modes detuning the frequencies. From these calculations it is evident that phase retardation effects reduce the amount of splitting for the symmetric hybrid mode. The phase retardation effect combined with the d-electron effect will force the symmetric plasmon mode of the

concentric nanoshell below the inner nanoshell plasmon mode. This combined effect is clearly seen in experimental data that will be presented in the next section.

6.3 Sample Preparation

Concentric gold nanoshells were fabricated using the synthetic route described in Chapter 3. Figure 6.8 shows a series of SEM images depicting the growth of a concentric gold nanoshell beginning with the preformed gold nanoshell particle (Fig. 6.8a) the silica encapsulation (Fig. 6.8b), attachment and initial growth of the small gold colloid (Fig. 6.8c) and the complete second gold shell (Fig. 6.8d). Near and mid infrared extinction spectra were measured using a Nicolet Magna-IR 560. An XT-KBr beamsplitter was used to span the range of near to mid infrared wavelengths. In order to measure the infrared spectra, nanoshells were derivatized with a thiol (1-dodecandethiol, as described in Chapter 5) and then either suspended in carbon disulfide (CS_2) or chloroform (CHCl_3) in a 1 mm path length sealed cell (NIR) or dried and mixed with potassium bromide (KBr) and pressed into a pellet (NIR and MIR). While the chemical instability of core-shell particles in haloalkanes was demonstrated in Chapter 5, it was observed that the particles remain stable in CHCl_3 for an adequate time (>12 hrs) to perform a complete spectral analysis.

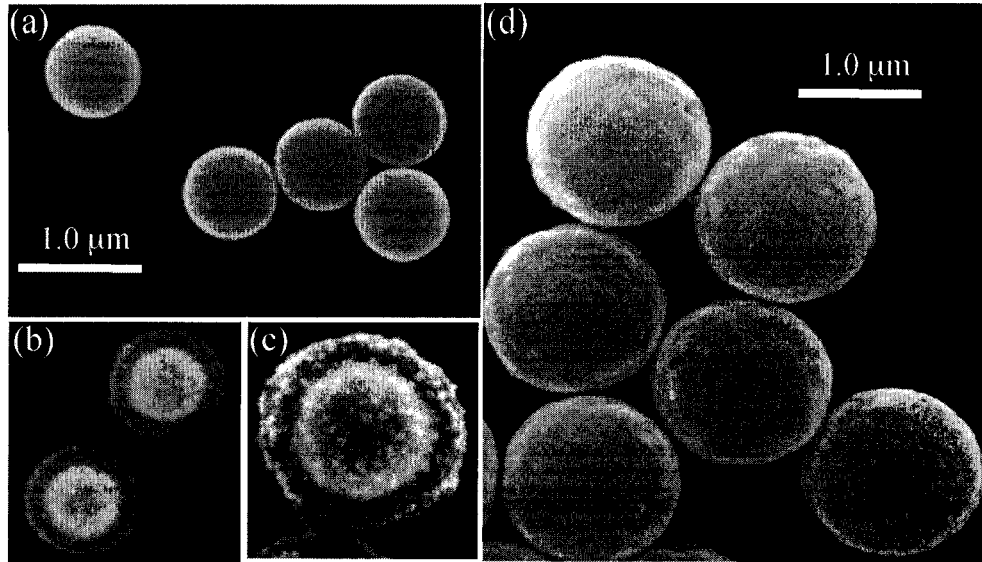


Figure 6.8: Set of SEM images depicting the concentric nanoshell fabrication process beginning with (a) a preformed nanoshell with a ~ 800 nm diameter. (b) The silica-encapsulated nanoshell with a ~ 240 nm thick silica layer (c) is then seeded with THPC-Au particles and (d) a final second gold shell is reduced onto the seeded surface resulting in a concentric nanoshell with an ~ 1.4 micron diameter.

6.4 Results and Discussion

Concentric nanoshells with a near-infrared plasmon response were fabricated using a preformed nanoshell particle constructed from a 160 nm diameter silica core with a 27 nm thick gold shell. Two concentric nanoshell geometries were investigated using different silica shell thickness to create a strong-coupling regime and a weak-coupling regime. The experimentally measured peak positions for the hybrid plasmon modes are plotted in Figure 6.9 for each regime and compared to the position of the theoretically calculated hybrid plasmon modes. In the strong-coupling regime the nanoshell is encapsulated in a 28 nm thick silica layer, onto which is grown a gold shell between 15 and 25 nm thick. The peak plasmon position of the two hybrid plasmon modes for this particle is plotted in Figure 6.9(a). The predicted and measured peak positions show excellent agreement. The peak position of the hybrid plasmon mode exhibits a strong

splitting with respect to the single-layer nanoshell plasmon modes owing to the relatively small separation distance between the two gold shells. The peak plasmon position for the weak-coupling regime is shown in Figure 6.9(b). In this weak-coupling regime a 48 nm thick silica layer is grown onto the previously stated nanoshell core. A gold shell between 10 – 20 nm thick is then grown to produce the measured extinction spectra. It is clear from this data that the hybrid plasmon modes exhibit a smaller degree of splitting with respect to the single nanoshell plasmon modes. The peak position of the hybrid modes are also red-shifted with respect to the single nanoshell modes due to the strong influence of phase retardation effects and interband transitions as described in the previous section.

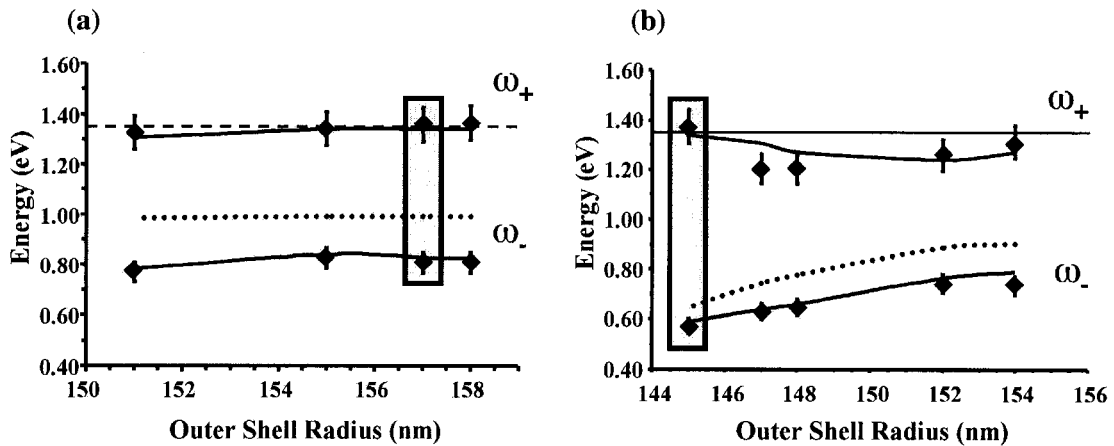


Figure 6.9: Experimentally measured peak plasmon positions (diamonds) compared to the theoretically predicted hybrid plasmon modes (solid lines). The symmetric and anti-symmetric modes are labeled for clarity. The straight solid line represents the experimentally measured inner shell plasmon mode, which is constant. The dotted line represents the calculated peak position of the outer shell plasmon mode as R_4 varies.

The actual spectra for the highlighted particles in Fig. 6.9(a) and 6.9(b) are shown in Figure 6.10. In this figure the measured spectra show excellent agreement with the theoretical fit using our classical electrodynamic model. In the strong-coupling regime,

Fig. 6.10(a), it is clear that the plasmon resonance exhibits a more complex structure due to the evolution of the hybrid plasmon modes. The concentric nanoshell plasmon in Figure 6.10(a) is red-shifted by 300 nm with respect to the plasmon resonance of the equivalent size single layer nanoshell. This shift is due to the “dipole in a nanocavity” configuration of the concentric nanoshell geometry, which couples the inner and outer nanoshell plasmon resonances and red-shifts the resonance of the composite nanostructure due to the hybridization of the plasmon resonance. This is compared with the plasmon resonance in the weak-coupling regime of the concentric nanoshell in Fig. 6.10(b). In this figure there is only a slight shift of the hybrid plasmon modes with respect to the single nanoshell modes indicating only a weak interaction between the inner and outer shell plasmons.

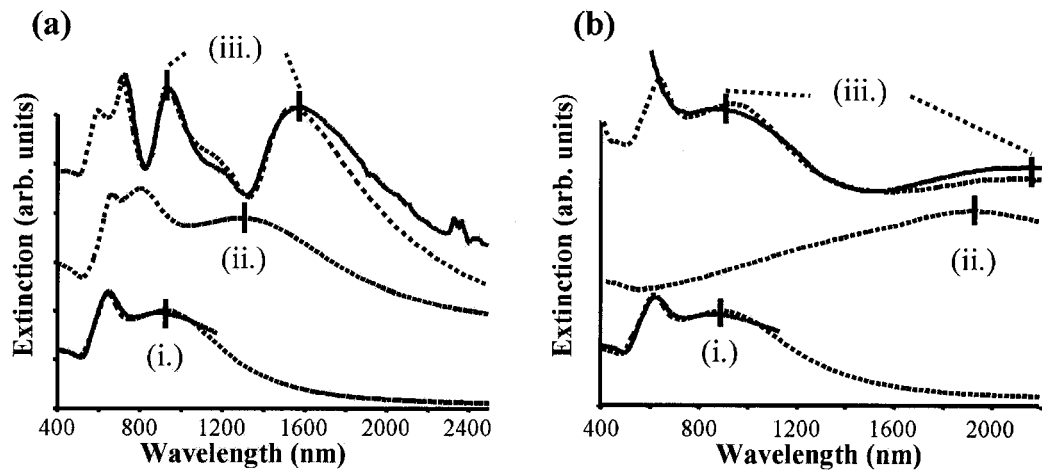


Figure 6.10: Experimental (solid) and theoretical (dotted) extinction spectra for concentric nanoshells in (a) the strong-coupling regime and (b) the weak-coupling regime. The lines indicate the peak position of the dipole resonance mode for the (i.) inner shell, (ii.) outer shell, and (iii.) concentric nanoshell particles.

The complex structure exhibited in the concentric nanoshell extinction spectrum in Fig. 6.10(a) is due to the hybridization of the higher order multipole modes, particularly the quadrupole and octupole modes of the inner and outer shell plasmon resonances. Figure

6.11 plots the hybrid multipole modes separately to show the contribution of these modes to the overall extinction spectrum. The major peaks of the extinction spectrum are labeled explicitly. The anti-symmetric (ω_-) quadrupole mode sits on top of the symmetric (ω_+) dipole mode, while both the hybrid octupole modes (ω_+ , ω_-) sit on top of the symmetric quadrupole mode (ω_-).

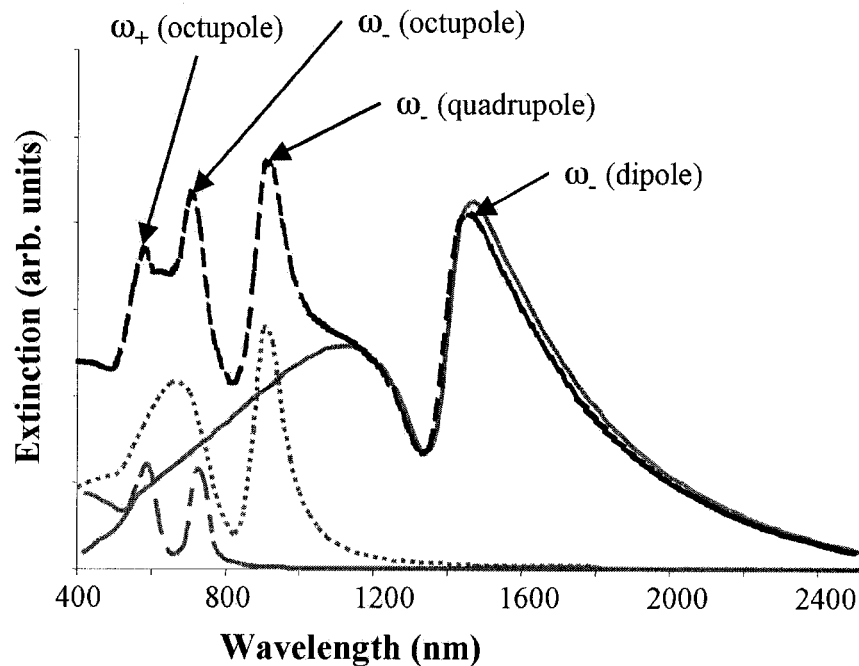


Figure 6.11: The complex, multi-peak structure of the concentric nanoshell in Fig. 6.10(a) is due to the hybridization of the higher order multipole modes. The dipole (solid gray), quadrupole (dotted gray), and octupole (dashed gray) resonant modes of the concentric nanoshell are plotted independently for clarity.

Construction of concentric nanoshells with an absorbance in the mid infrared region of the spectrum (> 3 microns) required a significant increase in the dimensions of the core silica particle. The initial single layer nanoshell particle was a core particle having a 792 nm diameter and a 22 nm thick gold shell. Subsequent silica encapsulation and silica layer growth resulted in a 236 nm thick silica shell followed by the growth of a 39 nm

thick gold shell. The infrared spectra for these particles are shown in Figure 6.12 with comparisons to Mie scattering theory. Both the nanoshell and concentric nanoshell particles have a strong mid infrared absorbance demonstrating the dynamic range of both the single-layer and multi-layer nanoshell particles. The spectra show the ability to reach into the mid infrared region utilizing either single or multi-layer nanoshell geometries. The single nanoshell particle has a strong plasmon resonance peak located at 3.5 microns while the concentric nanoshell has a strong peak at 5.8 microns. Each spectrum shows excellent agreement with Mie scattering theory calculations. This demonstrates that it is possible to span from the visible into the mid infrared region of the spectrum using nanoshell particles. Examination of the calculated spectra in Fig. 6.12 shows that there is a regime with essentially no coupling between the inner and outer nanoshell plasmons, where the concentric nanoshell plasmon resonance is virtually identical to that of a single shell particle of the same overall dimensions. Therefore, in the larger size regimes there is no apparent benefit to a multi-layer geometry to increase the spectral range of a nanoshell particle.

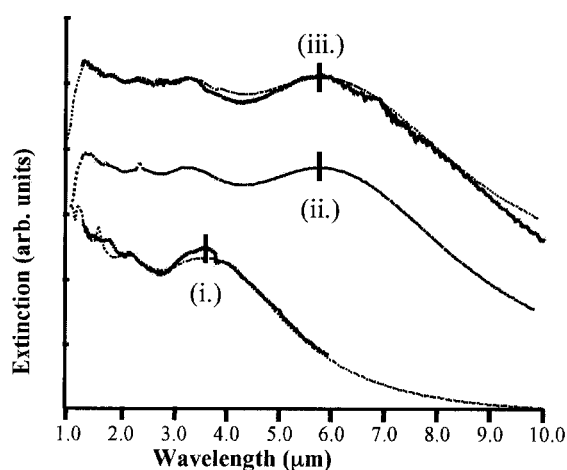


Figure 6.12: The theoretical and measured extinction spectra for a concentric nanoshell in a regime where there is no coupling between the inner and outer plasmon modes. The concentric nanoshell spectrum (iii.) appears the same as the single-layer nanoshell spectrum for the outer shell particle (ii.).

6.5 Conclusions

We have fabricated two different particles possessing nanoscale dimensions and a tunable plasmon resonance that can be placed over a broad range of the infrared spectrum (0.7 – 6 microns). Using a metal nanoshell as a platform for continued growth of dielectric and metal layers it was possible to fabricate a particle with a multi-layer, concentric sphere geometry. The optical properties of the multi-layer nanoshell are highly dependent on the overall size of the particle. For relatively small multi-layer nanoshells we have observed interesting optical effects owing to the nanoshell in a cavity regime where the overall optical properties of the particle are strongly influenced by the inclusion of the inner nanoshell. This can be explained in terms of the sphere-cavity model of plasmon hybridization. The individual plasmon resonances of the inner and outer shell are coupled resulting in a hybrid plasmon resonance with two distinct eigenmodes associated with the symmetric and anti-symmetric polarization of the two metal shells. However, the inclusion of the inner nanoshell does not appear to affect the optical properties of the particle when found within a large multi-layer nanoshell. This can be attributed to the complete decoupling of the two metal shell plasmons. The multi-layer nanoshell offers a unique geometry for the investigation of the electrodynamic properties of nanocavity systems containing strong optical absorbers. In the case of a purely plasmonic nanostructured particle these properties can be explained completely within the sphere-cavity model of plasmon hybridization.

Chapter VII: Deposition of Metal Nanoshells

7.1 Introduction

The controlled deposition of metal nanoshell particles into arrays is an area of great interest for the generation of photonic band-gap materials,^{35,36,88} waveguides,⁸⁹ and sensors.^{3,7,72,90} Solution-phase methods, such as sedimentation or convective assembly, are popular ways to approach the deposition of many nanoparticle systems.^{91,92} These methods work well for small metal particles or lightweight, dielectric particles with a controllable surface charge.⁹³⁻⁹⁵ Particularly there are three popular deposition techniques: electrostatic assembly where a nanoparticle with a controllable surface charge is deposited onto an oppositely charged surface, sedimentation where the natural gravity induced sedimentation of the particles is used to form arrays of particles, and electric-field assisted deposition uses an applied electric field to counteract gravitational sedimentation forces, or to directly manipulate a charged colloid, into an array. The direct application of these methods to nanoshells poses a number of problems.

All of the mentioned assembly techniques rely on a stable particle solution where the nanoparticles are highly dispersed and free from aggregation. This is most easily accomplished by controlling the surface charge on the particle while in solution. Most nanoparticles possess a surface charge inherent to their material properties. However, it is also possible to introduce a variable surface charge through the chemical functionalization of the nanoparticle surface. The charged particles are then highly stable in solution. The ionic double layer described by DLVO theory can be manipulated to

maintain a stable particle dispersion in solution (Chapter 3). The concentration of ions in solution determines the screening strength of this double layer and can easily be varied by changing solution pH.

In the case of electrostatic and electrophoretic deposition it is necessary to control the charge on the particle surface and for evaporation and sedimentation it is sometimes necessary to control the surface functionality of the particle to facilitate the transfer of the particles to more suitable solvents.⁹⁴ While a variety of molecular species exist for the surface derivatization of metal nanoparticles, a silica coating offers a useful chemical surface to expand the functionality of the particle. The silica surface itself represents a robust, charge-variable surface, which is easily transferable to a variety of solvents. The hydroxyl (-OH) groups on the silica surface provide a negative charge when the pH is varied basic, which causes deprotonation of these groups. The point of zero charge (PZC) on the silica surface has been measured at a pH between 2 and 3. The library of available silane molecules with different chemical head groups is large and includes thiols (-SH), methyls (-CH₃), amines (-NH₂), and carboxylates (-COOH, PZC at pH \approx 4). This results in a system where both the chemical functionality of the surface and its electric charge can be easily varied. Additionally it is possible to vary the thickness of the silica layer and therefore the extent of particle-particle interactions during and after assembly.

7.2 Electric-Field Assisted Deposition of Metal Nanoshells

Natural sedimentation has been widely used to create arrays of nanoparticles. This technique is limited to a small range of sizes where the rate of sedimentation is ideal. For silica particles the ideal size is around 200 – 500 nm in diameter. However, a similar size nanoshell is typically 50 – 100 times heavier due to the difference in density between gold and amorphous silica. If the nanoshell had an easily controlled surface charge then an electric field could be used to control the rate of sedimentation and counteract the gravitational force.⁹⁴ Using Stoke's Law one can see how much field to apply to achieve a specific velocity given solvent and particle parameters.

$$v = \frac{d^2(\rho_s - \rho_w)g}{18\eta} + uE \quad (1)$$

Where d is the particle diameter, ρ_s is the density of the particle, ρ_w is the density of water (or the appropriate solvent), g is the gravitational constant, and η is the solvent viscosity.

A cell consisting of a spacer layer (acrylic cuvette, Teflon, rubber) with a platinum top-electrode and an ITO-coated glass microscope slide, or silicon, as the substrate/bottom-electrode, was used for the electrodeposition of gold nanoshells. Different cell heights were experimented with and it was found that tall cells (> 1 cm) resulted in reproducible films. The taller cells rely on sedimentation to form the films whereas thin cells (< 3 mm) relied more on hydrodynamic forces at the surface to rearrange the particles after contact is made with the substrate. Smaller cells work well with lightweight polymer and metal oxide particles that move about readily on the surface, but nanoshells were found to be immobile once deposited onto the substrate. A diagram of the deposition apparatus is

depicted in Figure 7.1. A field was applied using DC potentials of 0.5 – 20 V from a variable power supply and the particles were monitored as they descended through the solution. Some groups have shown AC potentials to be beneficial in particle deposition, but this is typically used in dielectrophoretic trapping of single particles, where the electric field directly manipulates the particle into a location.⁹⁶ The change in height of the particle dispersion in solution was measured over time and this was used to calculate sedimentation velocity using equation 1. Solutions of silica-coated and bare nanoshells were prepared as described in Chapter 3 and the pH adjusted to 7 and 5, respectively, in order to maintain a surface charge on the particles. Figure 7.1(a) shows a graph of the particle height in solution over time for silica-coated gold nanoshells in a field applied from 5.8 V. The particle sedimentation velocity decreases by approximately 40% when the field is applied. Figure 7.1(b) shows the sedimentation rate for bare nanoshells in a field from 20 V. The particle velocity decreases by approximately 35 % when in the applied field. One reason for the large discrepancy in the required potential to decrease the nanoshell sedimentation velocity is the difference in the surface charges between the particles. The charge on the silica-coated nanoshells is inherent to the silica layer while the charge on the bare nanoshells is more dependent on the electric double layer. In an applied field the double layer will deform due to the induced polarization of the layer from the applied field. The electric double layer is also sensitive to hydrodynamic forces, which can cause the layer to distort as the particles move through solution.^{97,98}

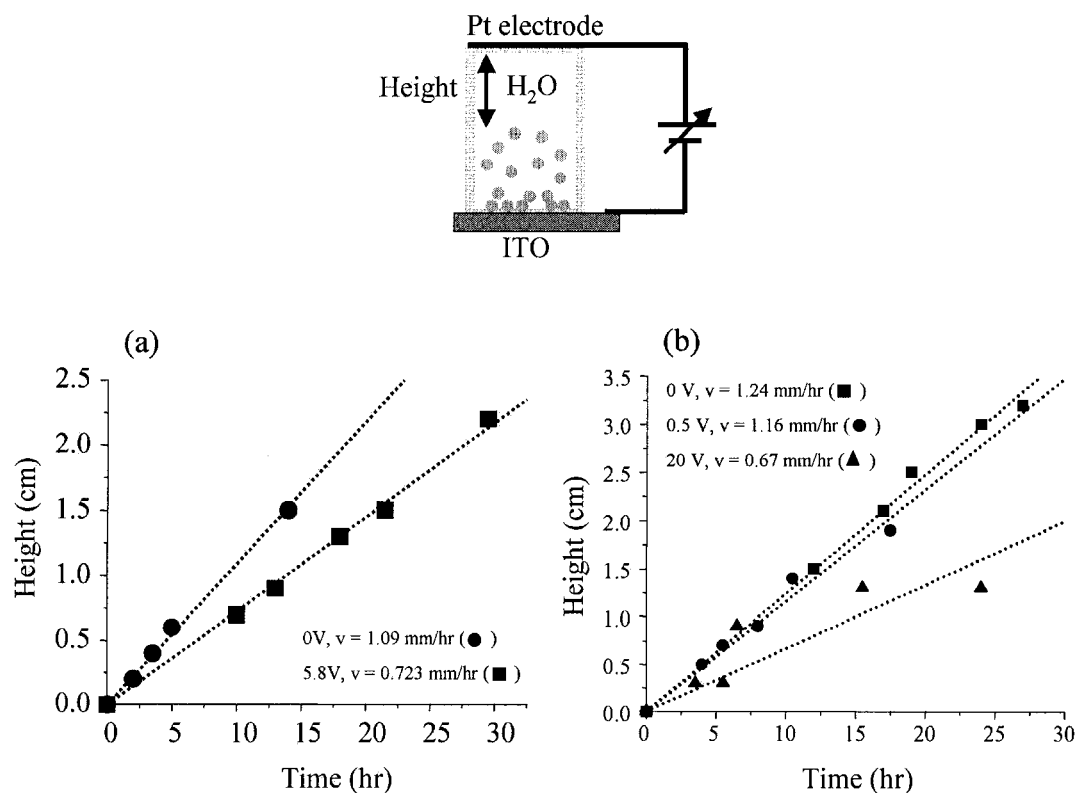


Figure 7.1: Schematic of an electrodeposition cell. The sedimentation rate for (a) silica-coated gold nanoshells and (b) bare gold nanoshells.

Two types of films were observed for coated and bare nanoshell deposition: semi-ordered and disordered. The films were characterized using electron microscopy (SEM) and spectroscopy (UV-Visible) to analyze the structural and optical properties of the films. When an electric field was applied an ordered structure was apparent in the nanoshell films. An example of an ordered and disordered film of silica-coated nanoshells is shown in Figure 7.2(a) and an ordered bare nanoshell film in Figure 7.2(b).

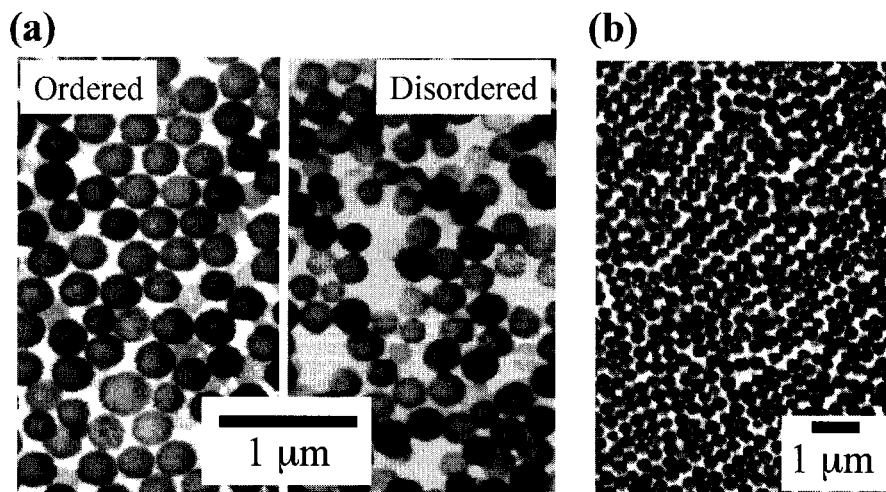


Figure 7.2: SEM images of (a) silica-coated gold nanoshells electrodeposited in ordered and disordered films and (b) bare gold nanoshells electrodeposited into an ordered film.

While no long-range order is evident, the particles are beginning to order and pack on short length scales. A change in the extinction spectra of the nanoshell films accompanies the deposition of an ordered film. The extinction spectra for different nanoshell films are displayed in Figure 7.3. The ordered films of coated nanoshells, Fig. 7.3(a), see a change in the extinction spectrum in the form of a peak blue-shifted with respect to the solution-phase nanoshell plasmon. For disordered films the spectrum retained the general shape of the nanoshell particles in solution. Both sets of spectra are slightly blue-shifted in peak position due to the change in refractive index going from water to air. A possible explanation for the change in the ordered nanoshell plasmon can be found in the interaction between multipole modes. Recent work has shown that specific multipole interactions can be enhanced between nanoparticles in an array.⁹⁹ This can result in a sharpening of a higher order multipole. Electrodeposited films were also prepared with bare nanoshells, which resulted in an ordered film with an extinction spectrum similar to the solution phase spectrum. The plasmon resonance of the ordered

bare nanoshell film has a distinctly sharp resonant mode seen in Fig. 7.3(b). This could be explained in terms of the multipole mode coupling suggested for the silica-coated nanoshell films. One characteristic of the multipole mode coupling is a sharpening of the plasmon mode. It is reasonable to assume that the particles in the bare nanoshell film can couple more efficiently due to their uninhibited interaction compared to the silica-coated or disordered particle films.

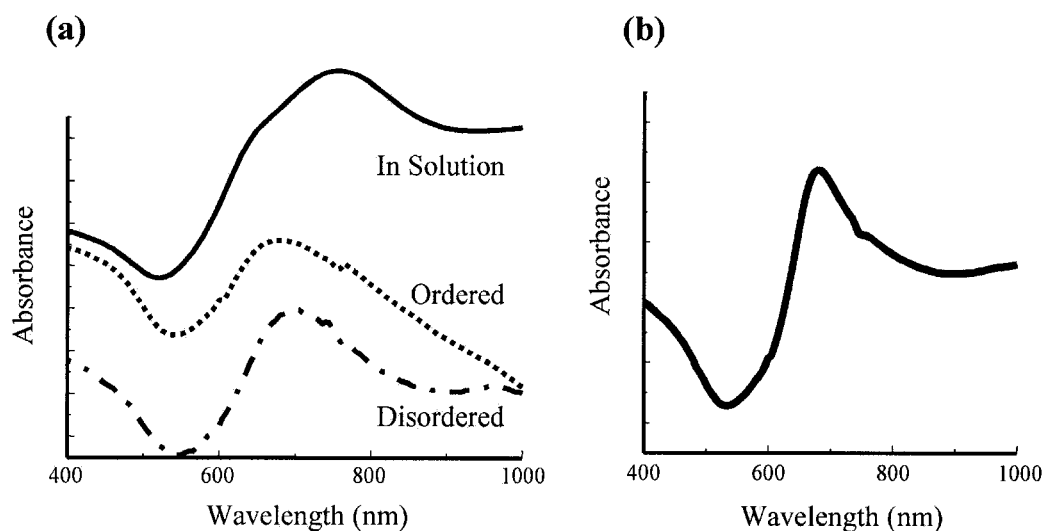


Figure 7.3: Extinction spectra for (a) silica-coated gold nanoshells and (b) bare gold nanoshells.

Typically, the ordered films possessed a shiny, metallic appearance, while the disordered films appeared dull, or matte as can be seen in Figure 7.4. This can be attributed to the inherent surface roughness of the films when comparing ordered to disordered films. In either case the films retained the color of the nanoshell particles in solution. The only noticed change in color of the films was observed when particles flocculated during the deposition process and in these cases the films appeared reddish-brown in color, consistent with the color of the flocculated shells in solution.

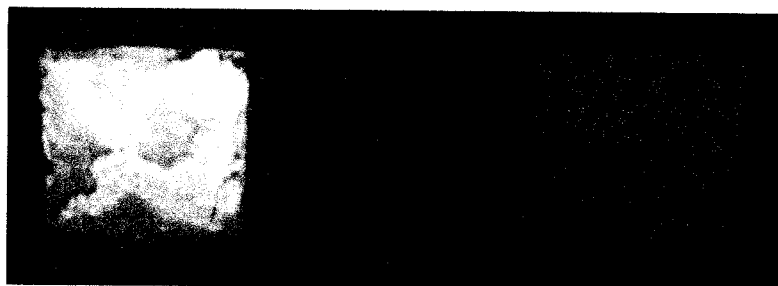


Figure 7.4: Picture of electrodeposited films of gold nanoshells. The film on the left corresponds to an ordered film while the film on the right is disordered.

7.3 Electrostatic Deposition of Metal Nanoshells

Nanoshell particles were also deposited using electrostatic interactions. In this method a surface is derivatized with a molecular monolayer in order to impart some electric charge using a suitable moiety. An oppositely charged nanoparticle can then be attached to the surface.¹⁰⁰⁻¹⁰² Electrostatic deposition of nanoshell particles was attempted using both the gold sulfide-gold and the silica-Au nanoparticle systems. Figure 7.5 depicts the electrostatic deposition scheme for gold sulfide-gold nanoshells. The deposition was accomplished by attaching an amino-silane to the surface of a glass microscope slide. At the correct pH the surface would have a positive electric charge due to the protonation of the amine head group. Using mercaptopropionic acid (MPA) the nanoshell surface can be negatively charged. The thiol bonds to the gold surface while at the correct pH the carboxylic acid group picks up a negative charge due to deprotonation of the acid. The nanoshell solution is easily adjusted to the correct pH using ion exchange resin (IXR). Slides were prepared using a method to make them hydrophilic.^{103,104} After cleaning the slides in strong acid (7:3 H_2SO_4 and H_2O_2) and base (5:1:1 H_2O , H_2O_2 , NH_4OH) solutions, the slides were then rinsed with water, methanol, and toluene. The hydrophilic

slides were then immersed in a dilute solution of N-2-aminoethyl-3-aminopropyl trimethoxysilane (TMS) in toluene and allowed to react ~12 hours. After this time the slides were washed with toluene, methanol, water, and sonicated to remove excess silane. Gold sulfide-gold nanoshells were prepared using a method described elsewhere,⁶⁵ derivatized with MPA to quench the growth reaction, and adjusted to a pH of 5 with IXR. The prepared slide was then dipped into a solution of MPA-derivatized nanoshells at a pH of 5.

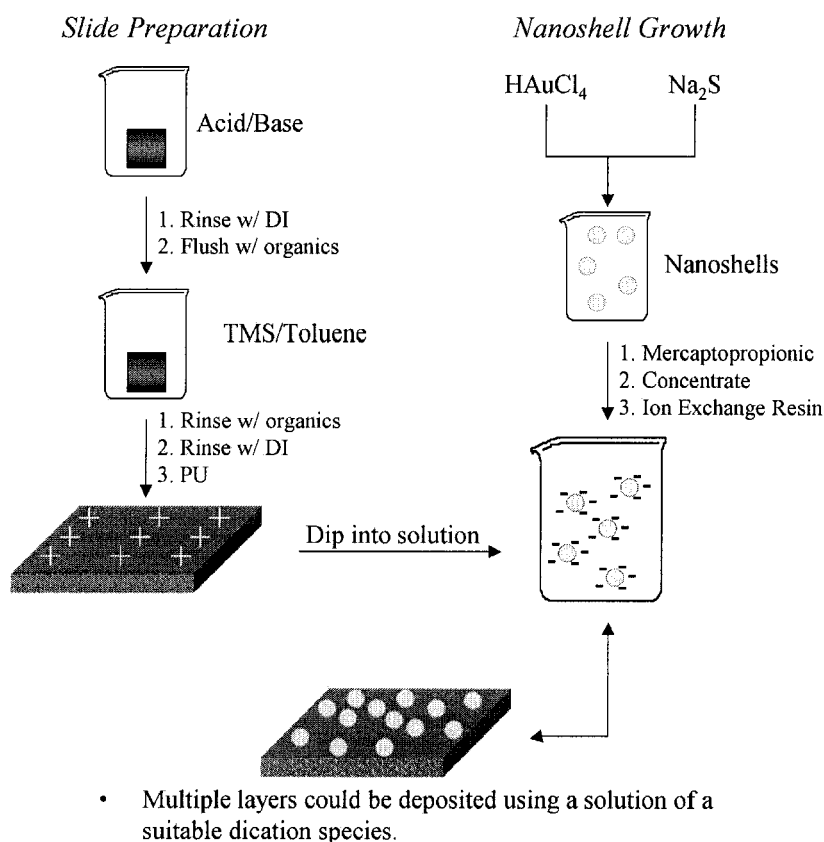


Figure 7.5: Schematic depicting the electrostatic deposition of nanoshells onto a flat substrate.

It was found that electrostatic deposition worked well for the gold sulfide-gold nanoshells, but not for silica-gold nanoshells due to the difference in size between the

two types of nanoparticles. The gold sulfide-gold particles are small (~ 50 nm) such that the electrostatic interaction is sufficient to bind the particles to the surface. In comparison the silica-gold nanoshell particles (> 100 nm) are too large and there is not a strong enough attraction to keep the particles on the surface. The size of the particles affects the surface area of the particle available to interact with the substrate and the forces influencing the particle in solution. Smaller particles are affected more by Brownian motion and will interact with the substrate more frequently with increased movement. The force between surfaces is affected by the radius of curvature and will be smaller for small particles and strong hydrodynamic forces are generated by large particles as they move through solution, which destabilizes the electric double layer and effects surface interactions through the generation of fluid currents.³⁹

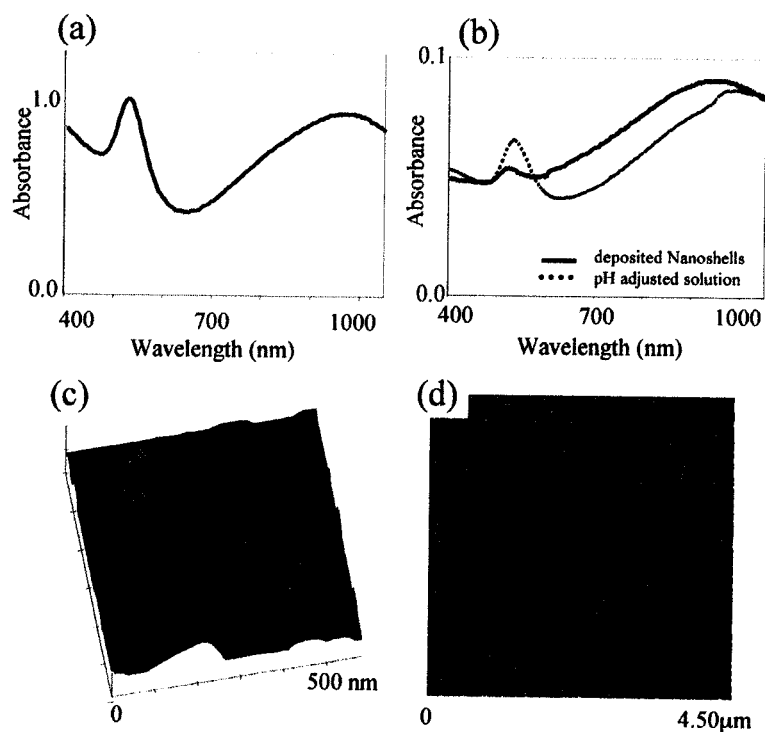


Figure 7.6: Extinction spectra and AFM images of electrostatically deposited nanoshells. (a) Gold sulfide-gold nanoshell extinction spectrum in solution. (b) Extinction spectra of nanoshells treated with IXR (dotted line) and deposited onto a prepared surface (solid line). (c) AFM image of nanoshells deposited onto a prepared surface after 10 min. and (d) 45 min.

An interesting effect observed in the deposition of gold sulfide-gold nanoshells is the increased deposition of nanoshells onto the surface and not gold colloid. The synthesis of the gold sulfide-gold nanoshells results in a large number of residual gold colloid (< 10 nm diameter). Figure 7.6 shows the extinction spectra for gold-sulfide gold nanoshells in solution and on a surface after electrostatic deposition. Figure 7.6(a) is the solution-phase nanoshell spectrum. The peak at about 550 nm is associated with the small gold colloid in solution. Using Mie scattering theory the volume of particles in solution was calculated to be $\sim 9.36 \times 10^{-4} \text{ cm}^3$ with a gold colloid concentration of 43 % v/v. Figure 7.6(b) shows the extinction spectrum of an IXR adjusted solution of nanoshells. The gold colloid peak has decreased and can be correlated to a concentration of about 4.6 % v/v gold colloid. The IXR used contains an amine moiety, which readily binds gold colloid. Furthermore, the IXR uses hydroxide ions (OH^-) coordinated to the amines to adjust the pH of a solution. The MPA-derivatized gold colloid will also coordinate to the amines due to the negative surface charge. This provides a strong argument for the uptake of the gold colloid in the IXR.

A significant decrease was seen in the gold colloid peak of the spectrum after electrostatic deposition onto a prepared surface. The extinction spectrum in Fig. 7.6(b) shows a further decrease in concentration to about 1.2 % v/v gold colloid. In this regime the concentration is determined from atomic force microscope (AFM) images of the nanoshell films. One possible explanation for this drastic decrease in the volume of the small gold colloid is the depletion of the colloid particles from the surface due to

hydrodynamic currents generated by the nanoshells upon approach to the substrate. The AFM images in Fig. 7.6(c) and 7.6(d) represent films generated by exposing the prepared substrates to the nanoshell solutions for 10 minutes and 45 minutes, respectively. The dense coverage generated over a relatively short time (~45 min.) indicates successful electrostatic attachment of the nanoshells to the substrate. Flat triangular and circular particles are also visible on the surface. These particles are by-products of the nanoshell synthesis and are also found in lower concentrations on the surface than in solution. This is most likely due to the oblate particle geometry limiting interaction with the surface. Multi-layers of nanoshells were attempted using diethylamine as a linking agent, but the molecule resulted in the destabilization of the nanoshell solutions. A possible solution to this problem is a layer-by-layer deposition approach using a suitable polyelectrolyte solution composed of a charged polymer.¹⁰¹

Other surfaces that have been used in the electrostatic deposition of nanoshell particles include polyethylene sheets and sapphire. Hydrophobic polyethylene sheets can be oxidized using a chromic acid solution ($\text{CrO}_3/\text{H}_2\text{O}/\text{H}_2\text{SO}_4$ 29/42/29 % wt).^{105,106} Immersing a polyethylene sheet in the chromic acid solution results in a 30 % oxidation of the surface with carboxylic acid groups rendering the surface hydrophilic. The carboxylate groups can be used in the electrostatic deposition of nanoshells by functionalizing the nanoshell surface with an amine moiety. The amine terminated nanoshell surface will be oppositely charged to the carboxylate group in solution allowing for nanoshell deposition. Sapphire ($\alpha\text{-Al}_2\text{O}_3$) can also be used as a substrate for electrostatic deposition due to its inherent surface charge. A sapphire surface possesses

an inherent charge without any further preparation. The PZC of sapphire is between a pH of 5 and 6.¹⁰⁷ Nanoshells have been successfully deposited onto sapphire using an electrostatic approach.

7.4 Summary

Metal nanoshells can be deposited into arrays of particles on flat substrates using both electric field assisted and electrostatic deposition methods. In the case of electric-field assisted assembly both silica-coated and bare nanoshells have been successfully deposited into arrays. These nanoshell films can possess a small degree of order, which results from the decreased sedimentation rate due to the applied field. The ordered films possess interesting optical properties, which may be described by multipole resonance coupling within the array. However, accurate description of this system requires further experimental investigation. The disordered nanoshell films appear to retain the extinction property of the individual nanoshells unless the particle dispersion is destabilized during deposition.

Electrostatic deposition has also been successful in the assembly of nanoshell films. Nanoshell particles have been assembled on various substrates including glass, polyethylene, and sapphire. However, this process seems to be limited to smaller nanoshell particles due to problems arising from forces acting on larger particles in solution. Both electrostatic and electric field assisted assembly have been applied to the fabrication of asymmetric nanoparticles called nanocaps and nanocups. In the fabrication

of nanocaps and nanocups, silica nanoparticles were deposited onto substrate mask to control the growth of an asymmetric metal shell.⁶⁶

Chapter VIII: Summary and Impact

This work has investigated the fabrication and optical properties of a new plasmonic nanostructure termed the concentric nanoshell. The concentric nanoshell particle consists of a multi-layer nanostructure with a dielectric-metal-dielectric-metal composition. Specifically, a particle with a silica core, an inner gold shell layer, a silica spacer layer, and a second gold shell layer has been fabricated. The multi-layer particle is fabricated using a gold nanoshell as a substrate for the deposition of the additional layers. The gold nanoshell is fabricated from a monodisperse silica core that has a strong plasmon resonance. The strength of the plasmon resonance is dependent on the quality of the nanoshell solution and the quality of the gold shell. The solution quality is dependent on monodisperse silica cores, which allow for the growth of a uniform gold shell on all particles in solution using electroless metallization techniques. The gold shell quality is dependent on the rapid reduction of a continuous gold shell onto the surface of the silica core. This is accomplished using small gold nanoparticles as nucleation sites for the electroless metallization. Increasing the ionic strength of the gold nanoparticle solution when mixed with the silica core particles can maximize the coverage of gold nanoparticles. The appropriate choice of reducing agent can also affect the quality of the gold shell that is grown. It was found that formaldehyde (large particles) and hydroxylamine hydrochloride (small particles) are ideal agents for the electroless reduction of gold onto the seeded core particle.

The encapsulation of a gold nanoshell in a silica layer was found to be strongly dependent on the solution pH and reactant concentration. Furthermore, excess ionic species found in the nanoshell solution were found to adversely affect the silica growth reaction. Chemical modification of the gold nanoshell with an aminoalkoxysilane molecule facilitates the condensation of a thin, 4 – 10 nm, silica shell from a dilute silicate solution. This thin silica layer can then be increased in thickness using the Stöber method of silica growth. Relatively thick silica layers were found to increase the overall thermal stability of the nanoshell particles significantly with respect to a bare gold nanoshell. Silica-encapsulated gold nanoshells were found to be stable to temperatures up to about 750 °C. The silica-encapsulated nanoshell was also found to chemically stabilize the nanoshell particles. Nanoshells dispersed in haloalkanes, such as carbon tetrachloride or chloroform, were found to decompose over time. This was attributed to an attack at the amine-gold linkage in the nanoshell structure resulting in a highly reactive charge-transfer complex. In the case of concentric nanoshell fabrication the haloalkanes were found to attack the outer gold shell, but were unable to affect the inner gold shell due to the silica-encapsulation layer.

The silica-encapsulated gold nanoshell was used as a substrate for the reduction of a second gold shell. The resulting double shell particle possesses a complex plasmon resonance that is a sensitive function of the nanoparticle dimensions. By tuning the core-shell ratio of both the inner and outer shell and by changing the thickness of the silica spacer layer between the two gold shells, the plasmon resonance can be tuned from the visible into the mid-infrared region of the electromagnetic spectrum. Using the sphere-

cavity model of plasmon hybridization, the concentric nanoshell plasmon can be described as a hybrid plasmon arising from the interaction of the inner and outer shell plasmon resonances. The plasmon response of the particle follows with the interactions predicted using the sphere-cavity model and agrees quantitatively with Mie scattering theory.

Using electric field assisted deposition techniques silica-coated and bare gold nanoshells with a silica-gold composition can be deposited into dense arrays. These arrays possess interesting optical properties, which may be attributable to interactions between the multipole resonances of the nanoshell plasmon. Gold nanoshells can also be assembled using electrostatic interactions. Nanoshells can be deposited onto positive or negatively charged surfaces when functionalized with the opposite charge. Surfaces can be prepared using a variety of molecules that can be easily attached in monolayers on suitable surfaces such as glass, polyethylene, and sapphire. Amine functionalized surfaces can electrostatically bind gold nanoshells derivatized with carboxylate groups. Conversely, amine derivatized nanoshells can be attached to carboxylate functionalized surfaces. This can be achieved by controlling the charge on the surfaces simply by changing the pH of the nanoshell solution.

Metal nanoshells are a functional plasmonic nanostructure possessing a highly frequency agile optical response. The fabrication of nanoshell particles is a robust process resulting in nanoparticles that can easily be incorporated into a variety of applications. The development of a multi-layered nanoshell particle increases the functionality of the

nanoshell and allows the particles to be incorporated into a broader range of applications. The increased thermal and chemical stability of the silica-encapsulated nanoshell increases the effectiveness of the nanoshell system in thermal management, photonic, and chemical sensing applications. Thermally stable nanoshells could be incorporated into fluids or coatings to improve thermally sensitive electronic or mechanical components.^{10,12} Thermally stable nanoshells would also be viable in photonics applications where the nanostructure is subjected to high intensity laser powers.¹⁰⁸ The increased frequency range made accessible by the double shell geometry also offers significant benefits in surface enhanced Raman, surface enhanced infrared, and fluorescence enhancement spectroscopies. The incorporation of an optically active (Raman, fluorescent, IR) moiety in the silica layers of the multi-layer particle could be used for the detection of chemical species. Nanoshells with molecularly embedded dielectric layers could also be used for sensor tags in various biological diagnostic assays.

The experimental realization of the concentric nanoshell system and the nature of the hybrid plasmon resonance lend strong support to the application of the sphere-cavity model in the description of plasmonic nanostructures. The simple model for plasmon interactions is akin to molecular orbital theory and likens the interactions of plasmons to the mixing of atomic orbitals in a molecular system. The ramification of this model is that plasmonic structures, such as core-shell, nearest-neighbor, or metallodielectric systems can be described by the interaction of simple sub-units of the nanostructure. This imparts another powerful tool to the design and fabrication of functional plasmonic nanostructures.

Bibliography

- (1) Oldenburg, S. J.; Averitt, R. D.; Westcott, S.; Halas, N. J. *Chem. Phys. Lett.* **1998**, 288, 243.
- (2) Nicewarner-Pena, S. R.; Griffith-Freeman, R.; Reiss, B. D.; He, L.; Pena, D. J.; Walton, I. D.; Cromer, R.; Keating, C. D.; Natan, M. J. *Science* **2001**, 294, 137 - 141.
- (3) Haes, A. J.; Van Duyne, R. P. *J. Amer. Chem. Soc.* **2002**, 124, 10596 - 10604.
- (4) Maier, S. A.; Brongersma, M. L.; Kik, P. G.; Meltzer, S.; Requicha, A. A. G.; Atwater, H. A. *Adv. Mater.* **2001**, 13, 1501.
- (5) Sun, Y.; Xia, Y. *Anal. Chem.* **2002**, 74, 5297 - 5305.
- (6) Kneipp, K.; Kneipp, H.; Itzkan, I.; Dasari, R. R.; Feld, M. S. *Chem. Rev.* **1999**, 99, 2957 - 2975.
- (7) Haynes, C. L.; Van Duyne, R. P. *J. Phys. Chem. B* **2003**, ACS ASAP.
- (8) Jackson, J. B.; Westcott, S. L.; Hirsch, L. R.; West, J. L.; Halas, N. J. *App. Phys. Lett.* **2003**, 82, 257.
- (9) Sershen, S. R.; Westcott, S. L.; Halas, N. J.; West, J. L. *J. Biomed. Mat. Res.* **2000**, 51, 293.
- (10) Sershen, S. R.; Westcott, S. L.; Halas, N. J.; West, J. L. *App. Phys. Lett.* **2002**, 80, 4609.
- (11) Westcott, S. L.; Averitt, R. D.; Wolfgang, J. A.; Nordlander, P.; Halas, N. J. *J. Phys. Chem. B* **2001**, 105, 9913 - 9917.
- (12) Eastman, J. A.; Choi, S. U. S.; Li, S.; Yu, W.; Thompson, L. J. *App. Phys. Lett.* **2001**, 78, 718 - 720.

- (13) Mie, G. *Ann. Phys.* **1908**, 24, 377.
- (14) Aden, A. L.; Kerker, M. *J. Appl. Phys.* **1951**, 22, 1242.
- (15) Stober, W.; Fink, A.; Bohn, E. *J. Coll. Inter. Sci.* **1968**, 26, 62-69.
- (16) van Blaaderen, A.; Vrij, A. *Langmuir* **1992**, 8, 2921-2931.
- (17) Moran, C. E.; Hale, G. D.; Halas, N. J. *Langmuir* **2001**, 17, 8376.
- (18) Prodan, E.; Lee, A.; Nordlander, P. *Chem. Phys. Lett.* **2002**, 360, 325 - 332.
- (19) Mulvaney, P. *Langmuir* **1996**, 12, 788- 800.
- (20) van der Hulst, H. C. *Light Scattering by Small Particles*; John Wiley and Sons: New York, 1957.
- (21) Kreibig, U.; Vollmer, M. *Optical Properties of Metal Clusters*; Springer-Verlag: New York, 1995; Vol. 1.
- (22) Bohren, C. F.; Huffman, D. R. *Absorption and Scattering of Light by Small Particles*; Wiley: New York, 1983.
- (23) Kittel, C. *Introduction to Solid State Physics*; Wiley: New York, 1956.
- (24) Westcott, S. L.; Jackson, J. B.; Radloff, C.; Halas, N. J. *Phys. Rev. B* **2002**, 66, 155431.
- (25) Sarkar, D.; Halas, N. J. *Phys. Rev. E* **1997**, 56, 1102.
- (26) Sarkar, D. In *Electrical and Computer Engineering*; William Marsh Rice University: Houston, 1997.
- (27) Oldenburg, S. J. In *Applied Physics*; William Marsh Rice University: Houston, 1999.

- (28) Johnson, P. B.; Christy, R. W. *Phys. Rev. B* **1972**, *6*, 4370.
- (29) Raether, H. *Excitation of Plasmons and Interband Transitions by Electrons*; Springer: Berlin, 1980; Vol. 88.
- (30) Prodan, E.; Nordlander, P. *Chem. Phys. Lett.* **2002**, *352*, 140-146.
- (31) Granqvist, C. G.; Hunderi, O. *Z. Phys. B.* **1978**, *30*, 47-51.
- (32) Sinzig, J.; Quinten, M. *Appl. Phys. A* **1994**, *58*, 157-162.
- (33) Liz-Marzan, L. M.; Giersig, M.; Mulvaney, P. *Langmuir* **1996**, *12*, 43229 - 44335.
- (34) Osseo-Asare, K.; Arriagada, F. J. *Colloids and Surfaces* **1990**, *50*, 321-339.
- (35) Jiang, P.; Bertone, J. F.; Colvin, V. L. *Science* **2001**, *291*, 453-457.
- (36) Denkov, N. D.; Velev, O. D.; Kralchevsky, P. A.; Ivanov, I. B.; Yoshimura, H.; Nagayama, K. *Nature* **1993**, *361*, 26.
- (37) Kanan, S. M.; Tze, W. T. Y.; Tripp, C. P. *Langmuir* **2002**, *18*, 6623-6627.
- (38) Duff, D. G.; Baiker, A.; Edwards, P. P. *Langmuir* **1993**, *9*, 2301 - 2309.
- (39) Evans, D. F.; Wennerstrom, H. *The Colloidal Domain: where physics, chemistry, biology, and technology meet*; Wiley-VCH: New York, 1994.
- (40) Kooij, E. S.; Martijn, E. A.; Wormeester, H.; Poelsema, B. *Langmuir* **2002**, *18*, 7677-7682.
- (41) Pawlow, P. *Z. Phys. Chem.* **1909**, *65*, 1.
- (42) Ercolessi, F.; Andreoni, W.; Tosatti, E. *Phys. Rev. Lett.* **1991**, *66*, 911.
- (43) Vanfleet, R.; Mochel, J. M. *Surf. Sci.* **1995**, *341*, 40.

- (44) Couchman, P. R.; Jesser, W. A. *Nature* **1977**, *269*, 481.
- (45) Castro, T.; Reifengerger, R.; Choi, E.; Andres, R. P. *Phys. Rev. B* **1990**, *42*, 8548.
- (46) Buffat, P.; Borel, J. *Phys. Rev. A* **1976**, *13*, 2287.
- (47) Allen, G. L.; Bayles, R. A.; Gile, W. W.; Jesser, W. A. *Thin Solid Films* **1986**, *144*, 297.
- (48) Correa-Duarte, M. A.; Giersig, M.; Liz-Marzan, L. M. *Chem. Phys. Lett.* **1998**, *286*, 497.
- (49) Alejandro-Arellano, M.; Ung, T.; Blanco, A.; Mulvaney, P.; Liz-Marzan, L. M. *Pure Appl. Chem.* **2000**, *72*, 257.
- (50) Bruchez, M.; Moronne, M.; Gin, P.; Weiss, S.; Alivisatos, A. P. *Science* **1998**, *281*, 2013.
- (51) Ung, T.; Liz-Marzan, L. M.; Mulvaney, P. *Langmuir* **1998**, *14*, 3740.
- (52) Li, T.; Moon, J.; Morrone, A. A.; Mecholsky, J. J.; Talhman, D. R.; Adair, J. H. *Langmuir* **1999**, *15*, 4328.
- (53) Oldenburg, S. J.; Hale, G. D.; Jackson, J. B.; Halas, N. J. *Appl. Phys. Lett.* **1999**, *75*, 1063.
- (54) Oldenburg, S. J.; Jackson, J. B.; Westcott, S. L.; Halas, N. J. *Appl. Phys. Lett.* **1999**, *75*, 2897.
- (55) Brown, K. R.; Lyon, L. A.; Fox, A. P.; Reiss, B. D.; Natan, M. J. *Chem. Mater.* **2000**, *12*, 314.
- (56) Pham, T.; Jackson, J. B.; Halas, N. J.; Lee, T. R. *Langmuir* **2002**, *18*, 4915 - 4920.
- (57) Lautenberger, W. J.; Jones, E. N.; Miller, J. G. *J. Amer. Chem. Soc.* **1968**, *90*, 1110 - 1115.

- (58) Jones, E. N.; Lautenberger, W. J.; Willermet, P. A.; Miller, J. G. *J. Amer. Chem. Soc.* **1970**, *92*, 2946 - 2949.
- (59) Biaselle, C. J.; Miller, J. G. *J. Amer. Chem. Soc.* **1974**, *96*, 3813 - 3816.
- (60) Willermet, P. A.; Miller, J. G. *J. Phys. Chem.* **1976**, *80*, 2473 - 2477.
- (61) Schmidt, U. C.; Osteryoung, J. G. *J. Electrochem. Soc.* **1997**, *144*, 3091 - 3095.
- (62) Mizukoshi, Y.; Okitsu, K.; Maeda, Y.; Yamamoto, T. A.; Oshima, R.; Nagata, Y. *J. Phys. Chem. B* **1997**, *101*, 7033 - 7037.
- (63) Bahnik, D. A.; Person, W. B. *J. Chem. Phys.* **1968**, *48*, 1251 - 1261.
- (64) Love, J. C.; Gates, B. D.; Wolfe, D. B.; Paul, K. E.; Whitesides, G. M. *Nano Letters* **2002**, *2*, 891-894.
- (65) Averitt, R. D.; Sarkar, D.; Halas, N. J. *Phys. Rev. Lett.* **1997**, *78*, 4217.
- (66) Charnay, C.; Lee, A.; Man, S. Q.; Moran, C. E.; Radloff, C.; Bradley, R. K.; Halas, N. J. *J. Phys. Chem. B*, **2003**, ASAP
- (67) Chen, S.; Fan, Z.; Carroll, D. L. *J. Phys. Chem. B* **2002**, *106*, 10777-10781.
- (68) Graf, C.; van Blaaderen, A. *Langmuir* **2002**, *18*, 524 - 534.
- (69) Huynh, W. U.; Dittmer, J. J.; Alivisatos, A. P. *Science* **2002**, *295*, 2425-2427.
- (70) Jackson, J. B.; Halas, N. J. *J. Phys. Chem. B* **2001**, *105*, 2743.
- (71) Jana, N. R.; Gearheart, L.; Murphy, C. J. *J. Phys. Chem. B* **2001**, *105*, 4065-4067.
- (72) Jensen, T. R.; Schatz, G. C.; Van Duyne, R. P. *J. Phys. Chem. B* **1999**, *103*, 2394-2401.

- (73) Kobayashi, Y.; Salgueirina-Maceira, V.; Liz-Marzan, L. M. *Chem. Mat.* **2001**, *13*, 1630 - 1633.
- (74) Maillard, M.; Giorgio, S.; Pileni, M. P. *J. Phys. Chem. B.* **2003**, *107*, 2466-2470.
- (75) Manna, L.; Scher, E. C.; Alivisatos, A. P. *J. Am. Chem. Soc.* **2000**, *122*, 12700-12706.
- (76) Pastoriza-Santos, I.; Liz-Marzan, L. M. *Nano Lett.* **2002**, *2*, 903-905.
- (77) Sun, Y.; Mayers, B. T.; Xia, Y. *Nano Letters* **2002**, *2*, 481-485.
- (78) Sun, Y.; Xia, Y. *Science* **2002**, *5601*, 2176-2179.
- (79) Jana, N. R.; Gearheart, L.; Murphy, C. J. *Langmuir* **2001**, *17*, 6782-6786.
- (80) Jana, N. R.; Gearheart, L.; Murphy, C. J. *Chem. Mater.* **2001**, *13*, 2313-2322.
- (81) Jana, N. R.; Gearheart, L.; Murphy, C. J. *Chem. Comm.* **2001**, 617-618.
- (82) Nikoobakht, B.; El-Sayed, M. A. *Chemistry of Materials* **2003**, *15*, 1957-1962.
- (83) Wundke, K.; Auxier, J.; Schülzgen, A.; Peyghambarian, N. *Appl. Phys. Lett.* **1999**, *75*, 3060-3062.
- (84) Malyarevich, A. M.; Denisov, I. A.; Savitsky, V. G.; Yumashev, K. V.; Lipovskii, A. A. *Appl. Opt.* **2000**, *39*, 4345-4347.
- (85) Gerion, D.; Pinaud, F.; Williams, S. C.; Parak, W. J.; Zanchet, D.; Weiss, S.; Alivisatos, A. P. *J. Phys. Chem. B* **2001**, *105*, 8861-8871.
- (86) Radloff, C.; Halas, N. J. *Appl. Phys. Lett.* **2001**, *79*, 674-676.
- (87) Enderlein, J. *Appl. Phys. Lett.* **2002**, *80*, 315-317.

- (88) Pieranski, P. *Contemp. Phys.* **1983**, *24*, 25-73.
- (89) Lal, S.; Taylor, R. N.; Jackson, J. B.; Westcott, S. L.; Nordlander, P.; Halas, N. J. *J. Phys. Chem. B* **2002**, *106*.
- (90) Velev, O. D.; Kaler, E. W. *Langmuir* **1999**, *15*, 3693-3698.
- (91) Dimitrov, A. S.; Nagayama, K. *Langmuir* **1996**, *12*, 1303-1311.
- (92) Park, S. H.; Qin, D.; Xia, Y. *Adv. Mater.* **1998**, *10*, 1028-1032.
- (93) Jiang, P. In *Chemistry*; William Marsh Rice University: Houston, 2001.
- (94) Holgado, M.; Garcia-Santamaria, F.; Blanco, A.; Ibisate, M.; Cintas, A.; Miguez, H.; Serna, C. J.; Molpeceres, C.; Requena, J.; Mifsud, A.; Meseguer, F.; Lopez, C. *Langmuir* **1999**, *15*, 4701-4704.
- (95) Dushkin, C.; Miwa, T.; Nagayama, K. *Chem. Phys. Lett.* **1998**, *285*, 259-265.
- (96) Bezryadin, A.; Dekker, C.; Schmid, G. *Appl. Phys. Lett.* **1997**, *71*, 1273.
- (97) Trau, M.; Saville, D. A.; Aksay, I. A. *Science* **1996**, *272*, 706-709.
- (98) Trau, M.; Saville, D. A.; Aksay, I. A. *Langmuir* **1997**, *13*, 6375-6381.
- (99) Malynych, S.; Chumanov, G. *J. Am. Chem. Soc.* **2003**, *125*, 2896-2898.
- (100) Grabar, K. C.; Freeman, R. G.; Hommer, M. B.; Natan, M. J. *Anal. Chem.* **1995**, *67*, 735-743.
- (101) Fendler, J. H. *Chem. Mater.* **1996**, *8*, 1616-1624.
- (102) Lvov, Y.; Ariga, K.; Onda, M.; Ichinose, I.; Kunitake, T. *Langmuir* **1997**, *13*, 6195-6203.

- (103) Ferreira, M.; Rubner, M. F. *Macromolecules* **1995**, 28, 7107-7114.
- (104) Fou, A. C.; Rubner, M. F. *Macromolecules* **1995**, 28, 7115-7120.
- (105) Rasmussen, J. R.; Stedronsky, E. R.; Whitesides, G. M. *J. Am. Chem. Soc.* **1977**, 99, 4736-4745.
- (106) Price, G. J.; Keen, F.; Clifton, A. A. *Macromolecules* **1996**, 29, 5664-5670.
- (107) Antelmi, D. A.; Spalla, O. *Langmuir* **1999**, 15, 7478-7489.
- (108) Chang, S.; Shih, C.; Chen, C.; Lai, W.; Wang, C. R. *Langmuir* **1999**, 15, 701.